Nonlinear Three-Port Representation of PAs for Embedded Self-Calibration of Envelope-Dependent Dynamic Biasing Implementations

SMARJEET SHARMA[ID], **(Student Member, IEEE), AND**
NICOLAS G. CONSTANTIN[ID], **(Senior Member, IEEE)**
Department of Electrical Engineering, École de Technologie Supérieure, Montreal, QC H3C 1K3, Canada

Corresponding author: Smarjeet Sharma (smarjeet.sharma.1@ens.etsmtl.ca)

ABSTRACT This paper proposes a three-port power amplifier (PA) representation based on distinct sets of nonlinear complex polynomials that describe a combiner, a nonlinear baseband-to-RF converter and a nonlinear RF amplifying function, for processing the PA's input modulated signal and any envelope-dependent dynamic biasing signal. This novel representation of PA nonlinearities simplifies computation and renders possible analytical formulations to describe a 3-port PA system. It allows accurate prediction of the PA's output distortion components as a function of an input multi-tone excitation and a multi-tone dynamic biasing signal. The representation is intended for a context proposed, to the best of the authors' knowledge for the first time, and envisioned as promising for future mobile communication equipment – the automatic optimization of linearity performance in Radio Frequency Integrated Circuit (RFIC) PAs under any modulated excitation and employing envelope-dependent biasing, through implementation of embedded self-calibration within the transmitter front-ends. In this context, the representation introduced here compares favorably in terms of accuracy with respect to Volterra-based approaches and allows a simpler characterization, while the literature often points to the complexity inherent to Volterra-based approaches. The proposed representation allows the optimization of the PA's dynamic biasing for linearity improvement from one mobile unit to another through embedded self-calibration starting from quasi-static measurements alone of the PA's input/output power. Its applicability is highlighted through benchmarking against experimental results demonstrating accurate PA characterization for multiple PA platforms under different dynamic biasing techniques. In one implementation using an industry-designed GaAs PA, it accurately predicts the dynamic biasing adjustments to achieve more than 4dB reduction in the output intermodulation distortion (IMD_3). In another implementation using the recently introduced positive envelope feedback linearization scheme, the proposed representation allows, for the first time, analytically predicting the condition of closed-loop stability and the requirements for the feedback components with experimental verification.

INDEX TERMS Dynamic biasing, embedded self-calibration, linearity, multi-tone signals, positive envelope feedback, power amplifier, three-port representation.

I. INTRODUCTION

The principle of dynamic biasing plays an important role in the design of many RFIC PA architectures. Dynamic biasing

commonly involves variation of the bias signal of the PA's RF transistors around its quiescent DC level as a function of a control signal, for improving its linearity-power efficiency trade-off. The control signal may be a function of the PA's average or instantaneous power level. For example, average power-dependent dynamic biasing is used to

The associate editor coordinating the review of this manuscript and approving it for publication was Haiwen Liu[ID].

improve the power added efficiency (PAE) of RF amplifiers in [1]–[4] and for PA gain regulation and efficiency optimization in [5]. Various open-loop and feed-forward implementations illustrated in [6]–[11] use a dynamic bias signal varying as a function of the PA's envelope power level. The recently proposed positive envelope feedback technique [12] demonstrates the use of instantaneous dynamic biasing in a closed-loop system to improve the PA's linearity-efficiency trade-off. Reference [13] shows the use of active FET elements to provide dynamic feedback for compensating the PA's gain compression at high power levels. Examples of closed-loop systems that use dynamic feedback are not limited to PAs. References [14] and [15] are examples of gain control through closed-loop negative feedback in variable gain amplifier (VGA) implementations.

The PA's response to an envelope varying RF signal is governed by complex nonlinear mechanisms. Dynamically changing the PA's bias as a function of the envelope adds further complexity to the PA's response. Moreover, the increasingly complex front-end PA modules in mobile transceivers may make use of different hardware states as part of a reconfiguration scheme (e.g. [16]). Such complex mechanisms inevitably introduce variations in the PA performances from one mobile unit to another. In this context, a self-calibration technique embedded within the mobile unit that would allow optimizing the dynamic biasing taking into account the performance variation from one unit to another would be of interest for current and future mobile wireless equipment. An example where embedded self-calibration would be useful is when the PA is subjected to dynamic biasing through the envelope-dependent modulation of the gate bias [12], [13] to improve the PAE-linearity trade-off. Embedded self-calibration within the mobile unit would then allow performing the necessary adjustments on each PA to reduce the spread in performance from one mobile unit to another, hence ensuring the best PAE-linearity trade-off in every unit.

To the best of the authors' knowledge, a method specifically for embedded self-calibration of envelope-dependent dynamic biasing in a PA module within a mobile unit has not been reported. Fig. 1 shows the embedded RF front-end self-calibration application that is envisioned in this paper. Here, the control signal V_{ctrl} determines the value of the PA's dynamic bias signal to be used at a particular power level. Its value is computed using a sufficiently accurate PA representation (X in Fig. 1). X (and hence the value of V_{ctrl}) is adjusted from one mobile unit to another starting from a minimum number of quasi-static power measurements over a narrow power range only, using *Input Probe* and *Output Probe* (the design of which is not addressed here). In this and other contexts that would require self-calibration, a simple PA representation X which accounts for a sufficiently high order of PA nonlinearity, which is straightforward to extract and store and which is suitable for embedding into mobile equipment for self-calibration (hence excluding commercially available tools/software) offers interesting possibilities.
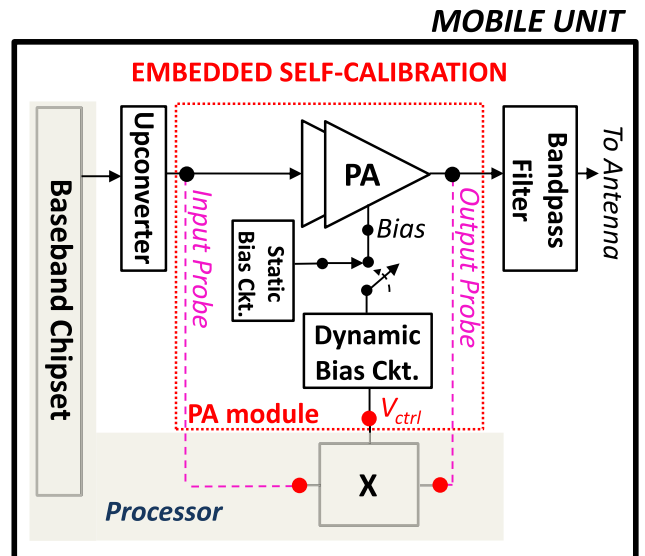

FIGURE 1. Proposed embedded self-calibration technique within the mobile unit in the RF front-end using the PA representation *X*. The control signal V_{ctrl} is synthesized using *X*, and determines the value of the dynamic bias signal at different power levels.

Among the nonlinear PA representations found in the literature [17]–[20], frequent references are drawn to the *Volterra series* given by the multi-dimensional time-domain convolution in (1) [18]. The full Volterra series (1) is well known for its ability to model memory effects arising from weakly nonlinear mechanisms in PAs and represents an exact mathematical model in theory.

$$y(t) = \sum_{n=1}^{\infty} \int_{-\infty}^{+\infty} \cdots \int_{-\infty}^{+\infty} \begin{array}{c} h(\tau_1, \ldots, \tau_n) \\ \{x(t-\tau_1) \ldots x(t-\tau_n)\} d\tau_1 \ldots d\tau_n \end{array}$$

(1)

However, higher-order Volterra kernels $h(\tau_1, \ldots, \tau_n)$ in (1), which are required to perfectly capture the PA's memory effects, present significant difficulties to extract due to the inherent complexity of the Volterra series [19]. Due to such difficulties, works based on Volterra series for representing PAs often limit themselves to first-order Volterra kernels only, under the assumption that higher-order Volterra kernels can be ignored without sacrificing the necessary accuracy. For example, the first-order approximation of (1) is used for the *modified* Volterra series applied to a *multi-tone* excitation in [18], as shown in (2).

$$y(t) \cong F[x(t)] + \int_{-\infty}^{+\infty} \begin{array}{c} g_1(x(t), \tau_1) \\ \{x(t-\tau_1) - x(t)\} d\tau_1 \end{array}$$

(2)

where $F[x(t)]$ represents the PA's quasi-static nonlinearity only.

In the context of embedded self-calibration, the advantages of PA representations using first-order Volterra series

over other equations-based representations is debatable. The need for simplicity in the calibration steps and the computation algorithms outweighs the requirement for mathematically exact formulations in this context. Moreover, even the extraction of first-order Volterra coefficients have been shown to present challenges [21], and the extraction of higher-order Volterra kernels can quickly become laboriously complex. Additionally, the use of higher-order Volterra-based PA representations in the context of re-tuning (during operation) from one mobile unit to another present difficulties in terms of complex training sequences starting from the low-order through to higher-order Volterra kernel extractions [22, Ch. 4]. Another key consideration is that the applicability of Volterra-based approach for closed-form analytical representation of closed-loop feedback systems such as [12]–[15] has not been demonstrated.

Here again, to the best of the authors' knowledge, a 3-port nonlinear PA representation that provides a viable alternative to the Volterra approach in the context of self-calibration of envelope-dependent dynamic biasing of a PA within a mobile unit, while offering comparable accuracy and with the added advantage of allowing a closed-form analytical representation of the 3-port embedded PA system, has not been demonstrated. The nonlinear PA representation we propose in this paper [23] addresses these needs by demonstrating:

(i) a 3-port analytical PA representation based on two distinct sets of nonlinear complex polynomials that describe a combiner, a nonlinear baseband-to-RF converter and a nonlinear RF amplifying function. It accurately captures the effects of dynamic biasing including memory effects under multi-tone excitation, and allows predicting linearity improvement in terms of IMD_3, as well as ACP reduction with a modulated signal.

(ii) the simplification of the computational requirements for PA characterization under envelope-based dynamic biasing, in particular for high-order nonlinearity and with comparable accuracy to earlier proposed Volterra-based approaches.

(iii) the simplification of the training sequence within the mobile unit for embedded self-calibration of the dynamic biasing mechanism.

(iv) a method for embedded optimization of dynamic biasing performances from one mobile unit to another.

(v) a closed-form analytical representation of open-loop and closed-loop envelope-based dynamic biasing, enabling the determination of closed-loop feedback parameters to ensure stability and optimal linearity.

The 3-port PA representation is derived with the use of a multi-tone input excitation and a multi-tone dynamic biasing signal, with arbitrary amplitude and phase for each tone, which allows taking into consideration high degree nonlinearities. It is well known that multi-tone representations may be strongly correlated to spectral regrowth under modulated excitations [24]–[26], and is also shown in a later section. Additionally, though the proposed 3-port representation is demonstrated for the PA's dynamic gate biasing here, it can be

used to represent other nonlinear dynamic mechanisms (such as supply modulation [18]).

Note that the formulations in [27] are based on a simple variable gain control, using only a *linear* processing of a multi-tone biasing signal and are applicable only for limited peak-to-average envelope power ($\sim$2.5dB). They are intended only for *estimating* IMD levels in feedback amplifiers during the PA's engineering development phase. Hence they do not suit embedded self-calibration during the operation of the mobile equipment. The 3-port PA representation proposed here is fundamentally different. It is based on the use of a combiner, a nonlinear baseband-to-RF converter and a nonlinear amplifying function, for the *nonlinear* processing of the dynamic bias signal. This allows *accurate* prediction of PA performances under larger peak-to-average excitation, with a distinct representation of the nonlinear transfer function from the baseband dynamic bias signal to the RF output signal, as required for embedded self-calibration.

In Section II, the proposed 3-port PA representation is described conceptually. In Section III, the mathematical form of the proposed PA representation is derived and the steps to extract the polynomial coefficients are given. Section IV verifies the exactness of the proposed 3-port representation through its bench-marking against an RFIC PA design within a simulation test-bench. The use of the 3-port representation for PA linearization under multi-tone as well as modulated input RF excitation is shown. The proposed concept of embedded self-calibration is also demonstrated. In one experimental implementation described in Section V, the proposed 3-port representation accurately predicts the necessary adjustment in dynamic biasing to achieve more than 4dB reduction in IMD_3 for an industry-designed GaAs PA. Section VI highlights the differences of the proposed PA representation with other state-of-the-art PA representations for dynamic biasing. It describes the relatively simple yet accurate characterization process of the proposed representation which favors its inclusion in embedded self-calibration applications. In a second experimental implementation described in Section VII, the proposed 3-port representation is applied to the recently introduced positive envelope feedback technique for PA linearization [12]. The proposed representation allows predicting the conditions for system stability as well as the design requirements of the feedback system components for optimum closed-loop PA performance. Section VIII is a brief discussion on some possible embedded self-calibration applications of both open-loop and closed-loop PAs using the 3-port representation.

II. DESCRIPTION OF THE PROPOSED 3-PORT PA REPRESENTATION FOR DYNAMIC BIASING

The block diagram shown in Fig. 2 represents a PA with its envelope-dependent control signal (e.g. supply modulation or dynamic biasing) held at $V_{ctrl} = V_{dc}$ i.e. under constant DC supply and biasing. A complex nonlinear polynomial G represents the PA's RF transfer function, and the output multi-tone signal V_o can be derived from the input multi-tone signal
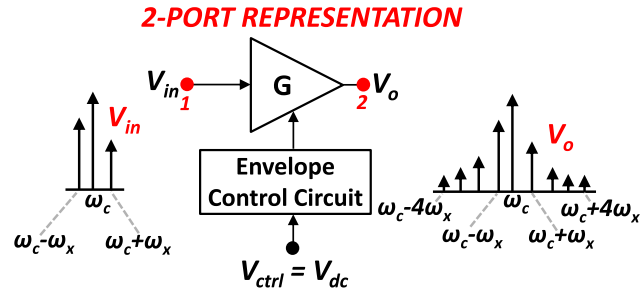
2-PORT REPRESENTATION

FIGURE 2. PA circuit under multi-tone excitation V_{in} and with $V_{ctrl} = V_{dc}$ (under constant DC supply and biasing). V_o represents the PA's output multi-tone signal. G is characterized with V_{ctrl} held at V_{dc}.

V_{in} with the help of (3).

$$v_o(t) = a_1 v_{in}(t) + a_3 v_{in}^3(t) + a_5 v_{in}^5(t) + \ldots \quad (3)$$

There is an inherent assumption that the PA output has a band-pass filter to limit the RF output spectrum to the frequency range of interest around ω_c. Therefore, the odd-order terms only are needed.

The complex coefficients a_1, a_3, a_5 etc. of polynomial G account for the PA's dynamic AM-AM and AM-PM behavior under $V_{ctrl} = V_{dc}$. It is shown in [28] that the memory effects of a PA and its impact on the PA's IMD characteristics in response to a multi-tone input excitation can be accurately captured using its dynamic AM-AM and AM-PM responses. Such memory effects are dependent on the carrier frequency ω_c, on the envelope amplitude variations of the modulated RF signal, and on the envelope frequency set by the two-tone frequency spacing ω_x. The set-up shown in Fig. 2 uses a three-tone excitation, hence the approximations detailed in [28] remain valid and the experimental set-up shown in [28, Fig. 2] can be used for the extraction of the PA's dynamic AM-AM and AM-PM, and therefore the complex coefficients of polynomial G.

The PA's RF transfer function G may be varied by modifying V_{ctrl}. Gain control by dynamically adjusting the PA's current through electronic control of its bias/supply circuit is one example of such a variation of G.

We now focus on dynamic biasing specifically, as an envelope-dependent mechanism. Fig. 3 shows an implementation where a dynamic bias signal V_e varying at the frequency of the input excitation tone spacing ω_x (as well as containing its higher-order harmonics) is applied to the PA. Such a dynamic bias signal is encountered in PA envelope-dependent biasing schemes [6]–[13].

Let us consider this change in the bias signal from $V_{ctrl} = V_{dc}$ to $V_{ctrl} = V_{dc} + V_e$. The input excitation V_{in} remains unchanged, and the change in the output multi-tone from V_o to V_o' under dynamic bias is captured by the change in the PA polynomial from G to G' (Fig. 3). G' therefore captures the PA's nonlinearities arising not only from an envelope modulated input signal, but also that due to a bias signal varying with the frequency of the PA's input/output envelope signal. However, any subsequent change in the PA's multi-tone bias
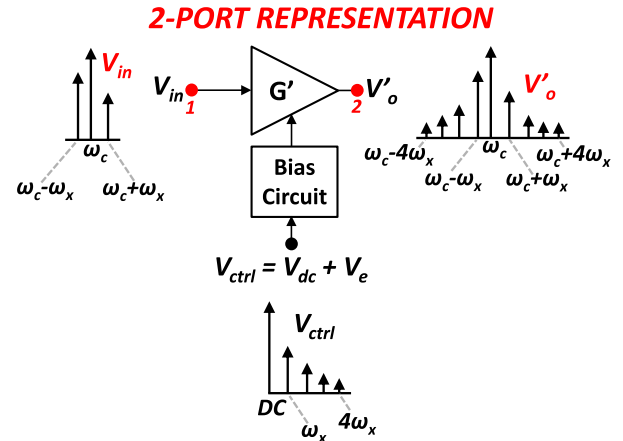
2-PORT REPRESENTATION

FIGURE 3. 2-port PA representation of Fig. 2 under dynamic bias. V_e is the dynamic multi-tone component of the bias signal and V_o' represents the PA's new multi-tone output signal. G' is the new complex polynomial characterized with the bias node excited by the dynamic bias signal $V_{ctrl} = V_{dc} + V_e$.

signal V_{ctrl} would necessitate the characterization of another new polynomial G'', which reflects the PA's nonlinearities with this new bias control.

Therefore, a PA representation that accounts for the PA's nonlinearities arising out of a change in its bias without resorting to a polynomial extraction routine with every such change offers an attractive alternative. It also provides an analytical means to understand the PA's nonlinearities as a function of its bias.
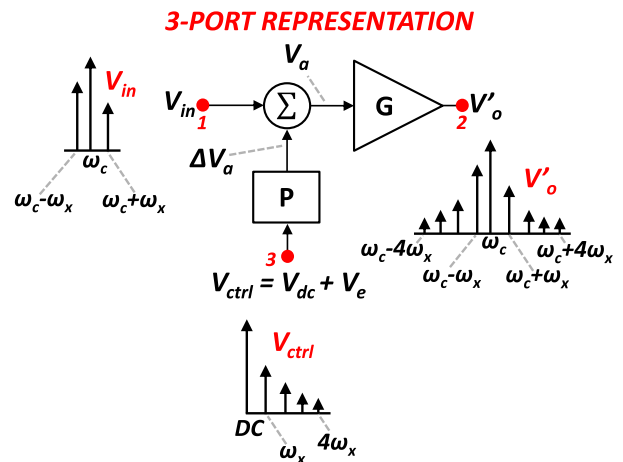
3-PORT REPRESENTATION

FIGURE 4. Proposed 3-port representation of PA under the dynamic biasing conditions shown in Fig. 3. Port 3 represents the PA's bias port. G is the same complex polynomial in Fig. 2 characterized with the PA's bias node held at $V_{ctrl} = V_{dc}$.

Fig. 4 shows our proposed 3-port representation for the PA under the dynamic bias of Fig. 3. The change in the polynomial from G to G' as described in Fig. 3 (resulting in a change of the output IMD tones from V_o to V_o') is equivalently accounted for in our proposed representation by an incremental change ΔV_a in the multi-tone input to the original polynomial G, where G is characterized with

$V_{ctrl} = V_{dc}$, i.e. $V_e = 0$. ΔV_a is derived from the dynamic biasing signal $V_{ctrl} = V_{dc} + V_e$ using a second nonlinear polynomial P (comprising a set of complex coefficients p, that define a multi-tone baseband to multi-tone RF conversion gain), and this ΔV_a signal, summed with V_{in} and applied to G, results in the new output signal V'_o. The summer and the node ΔV_a in Fig. 4 are not physically present in a typical PA architecture, but only represent an analytical equivalence.

It is worthwhile to note that PA tests and analysis based on multi-tone analysis are of significant help to designers [17]–[18], [24]–[26]. When limited to a few number of tones, such analyses offer intuitive insight and a relatively simple but accurate description of PA performances without dealing with the more complicated calculations involved when complex modulated excitation signals are used. Measurement data of multi-tone tests additionally allow easy and fast benchmarking using widely accepted PA performance measurements (such as IMD$_3$). Besides, the correlation of multi-tone measurements such as IMD$_3$ with other measurements used for modulated excitation signals (such as ACPR, EVM) is also documented [24], [25].

Additionally, it is well known that a PA representation that accounts for higher-order nonlinear contributions enhances the representation's accuracy; however, the difficulty of extracting higher-order kernels when using Volterra series (and given the challenges associated with even extracting first-order Volterra coefficients [21]) makes it prohibitively complex to use for embedded self-calibration. The 3-port PA representation proposed here overcomes this limitation by capturing higher-order contributions of the dynamic bias to the PA output with the help of lower-order polynomials that are easy to extract, thereby enhancing its accuracy.

For the purpose of illustrating this, consider our proposed 3-port PA representation in Fig. 4 limited to 3rd-order G (hence with coefficients a_1, a_3 only) and a 2nd-order P(hence with coefficients p_1, p_2) polynomials. Additionally, to simplify our analysis and without any loss of generality, consider a 1-tone RF excitation V_{in} at RF frequency ω_c and a 1-tone dynamic bias signal V_e (in addition to the quiescent DC value) at envelope frequency ω_x. As shown in Fig. 4, the output of the polynomial P being itself applied as input to the polynomial G, allows capturing an overall sixth-order nonlinear dependence of the PA's output signal V'_o on the dynamic bias V_e. It can be shown through expansion and simplification of (3) that the value of the third-order output tone $V'_o(\omega_c + 2\omega_x)$ shows this sixth-order nonlinear dependence as given by expression (4) below.

$$V'_o(\omega_c + 2\omega_x) = k_2 V_e^2 + k_3 V_e^3 + k_4 V_e^4 + k_5 V_e^5 + k_6 V_e^6 \quad (4)$$

where complex constants k_2, k_3, k_4, k_5 and k_6 stem from the coefficients of P and G. For example, the dependence of k_6 on a_3 and p_2 is shown in (5).

$$k_6 = (9/4) \cdot a_3 \cdot p_2^3 \quad (5)$$

Therefore, solving for a_1, a_3 and p_1, p_2 simultaneously allows capturing up to a sixth-order dependence of the PA's

output signal on V_e, despite P being limited to 2nd-order and G being limited to 3rd-order. The presence of even-order terms in (4), although G contains odd-order terms only, is due to the fact that P includes both even-order and odd-order baseband-to-RF contributions of the dynamic bias signal V_e to ΔV_a. These contributions are summed with V_{in} and then processed by G, resulting in odd as well as even-order terms in (4) that contribute to $V'_o(\omega_c + 2\omega_x)$. On the other hand, extracting the same 6th-order nonlinear dependence on the dynamic bias signal V_e when using Volterra-based PA representations would require increasing the order in equation (2), with the significant added complexity discussed before.

III. 3-PORT MATHEMATICAL REPRESENTATION
A. DERIVATION OF EQUATIONS
The three-tone input signal $v_{in}(t)$ applied to the PA input is represented by (6), and its equivalent bilateral form by (7).

$$v_{in}(t) = \sum_{i=-1}^{1} V_{in}(\omega_c + i\omega_x) \cdot \cos((\omega_c + i\omega_x) t + \theta_{\omega_c + i\omega_x}) \quad (6)$$

$$v_{in}(t) = \frac{1}{2} \sum_{\omega_r = \omega_c, -\omega_c} \left(\sum_{i=-1}^{1} V_{in}(\omega_r + i\omega_x) \cdot e^{j\theta_{\omega_r + i\omega_x}} \right. $$
$$\left. \cdot e^{j(\omega_r + i\omega_x)t} \right) \quad (7)$$

where $V_{in}(\omega_c + i\omega_x)$ and $\theta_{\omega_c + i\omega_x}$ represent the magnitude and phase respectively for each tone of $v_{in}(t)$. Note that $V_{in}(-\omega_c - i\omega_x) = V_{in}(\omega_c + i\omega_x)$, $\theta_{-\omega_c - i\omega_x} = -\theta_{\omega_c + i\omega_x}$ and j is the complex imaginary unit.

The multi-tone dynamic bias signal $v_e(t)$ applied to the PA bias terminal (and added to V_{dc}) is represented by (8).

$$v_e(t) = \sum_{i=1}^{m} V_e(i) \cdot cos(i\omega_x t + \Phi_i) \quad (8)$$

Here, m refers to the number of significant tones (excluding DC) present in the bias signal. For example, m equals 4 in Fig. 4 since the number of tones is 4, ranging from ω_x to $4\omega_x$. $V_e(i)$ and Φ_i represent the magnitude and phase respectively for each tone of $v_e(t)$.

The nonlinear baseband-to-RF transformation of $v_e(t)$ through polynomial P gives the incremental RF signal $\Delta v_a(t)$ as expressed by (9), and its bilateral form by (10).

$$\Delta v_a(t) = \sum_{i=-s}^{s} \Delta V_a(\omega_c + i\omega_x) \cdot \cos((\omega_c + i\omega_x) t + \gamma_{\omega_c + i\omega_x}) \quad (9)$$

$$\Delta v_a(t) = \frac{1}{2} \sum_{\omega_r = \omega_c, -\omega_c} \left(\sum_{i=-s}^{s} \Delta V_a(\omega_r + i\omega_x) \cdot e^{j\gamma_{\omega_r + i\omega_x}} \right.$$
$$\left. \cdot e^{j(\omega_r + i\omega_x)t} \right) \quad (10)$$

where $\Delta V_a(\omega_c + i\omega_x)$ and $\gamma_{\omega_c + i\omega_x}$ represent the magnitude and phase respectively for each tone of $\Delta v_a(t)$. Also, $\Delta V_a(-\omega_c - i\omega_x) = \Delta V_a(\omega_c + i\omega_x)$, $\gamma_{-\omega_c - i\omega_x} = -\gamma_{\omega_c + i\omega_x}$ and j is the complex imaginary unit. Here, s is related to the number of significant tones present in the

$\Delta v_a(t)$ signal, e.g. $s = 4$ indicates that there are 9 tones in the $\Delta v_a(t)$ signal, at frequencies $\omega_c - 4\omega_x, \omega_c - 3\omega_x \ldots 0 \ldots \omega_c + 3\omega_x, \omega_c + 4\omega_x$. The tones $\Delta V_a(\omega_r + i\omega_x) \cdot e^{j\gamma_{\omega_r + i\omega_x}}$ present in (10) are now expanded in terms of amplitude and phase to show the relationship of these tones to the multi-tone dynamic bias signal $v_e(t)$. With the help of coefficients p_{iql} of P, the value of the $\Delta v_a(t)$ tones is given by (11).

$$\{\Delta V_a(\omega_r + i\omega_x) e^{j\gamma_{\omega_r + i\omega_x}}\}|_{\omega_r = \omega_c}$$
$$= \sum_{q=1}^{m} \sum_{l=1}^{n} p_{iql} \{V_e(q) \cdot \cos(\phi_q)\}^l \quad (11)$$

Here, n refers to the order of the polynomial P. i varies from $-s$ to $+s$, where s is as defined in (10). $V_e(q)$, ϕ_q and m are defined in (8). To understand the indexing of p_{iql} in (11), consider (for example) the coefficient p_{312}. Here, index 2 in p_{312} represents that it captures the 2nd-order contribution of the $V_e(1)$ tone at frequency $1 \cdot \omega_x$ in the bias signal (given by index 1 in p_{312}), to the 3rd side-tone $\Delta V_a(\omega_c + 3\omega_x)$ (given by index 3 in p_{312}). The extraction procedure of the polynomial coefficients p_{iql} is detailed in Section III-B.

The incremental signal $\Delta v_a(t)$ is added to the input three-tone excitation $v_{in}(t)$ to obtain $v_a(t)$ as shown by (12).

$$v_a(t) = v_{in}(t) + \Delta v_a(t), \text{ i.e.}$$
$$v_a(t) = \frac{1}{2} \sum_{\omega_r = \omega_c, -\omega_c} \left(\sum_{i=-1}^{1} V_{in}(\omega_r + i\omega_x) \cdot e^{j\theta_{\omega_r + i\omega_x}} \cdot e^{j(\omega_r + i\omega_x)t} \right)$$
$$+ \frac{1}{2} \sum_{\omega_r = \omega_c, -\omega_c} \left(\sum_{i=-s}^{s} \left(\sum_{q=1}^{m} \sum_{l=1}^{n} p_{iql} \{V_e(q) \cdot \cos(\phi_q)\}^l \right) \right.$$
$$\left. \cdot e^{j(\omega_r + i\omega_x)t} \right) \quad (12)$$

The $v_a(t)$ signal given by (12) is now applied as input to the original complex polynomial G to obtain the output multi-tone signal $v_o'(t)$ under dynamic biasing.

$$v_o'(t) = a_1 v_a(t) + a_3 v_a^3(t) + a_5 v_a^5(t) \quad (13)$$

By replacing $v_a(t)$ in (13) with its value given by (12), expanding the resulting expression and then grouping the terms at each resulting frequency together gives closed-form expressions for the value of each tone present in the PA's output multi-tone signal, in terms of the parameters and signals listed in (12) and (13) i.e. in terms of the coefficients of G and P, and the signals $v_{in}(t)$ and $v_e(t)$. The number of terms as well as the explicit form of $v_o'(t)$ in (13) resulting from such an expansion being large, they are not shown here for the purpose of conciseness. However, after regrouping the output terms at the same frequency, a compact representation of the resulting $v_o'(t)$ output signal and its bilateral equivalent will have the form given by (14) and (15) respectively.

$$v_o'(t) = \sum_{i=-u}^{u} V_o'(\omega_c + i\omega_x) \cdot \cos((\omega_c + i\omega_x)t + \beta_{\omega_c + i\omega_x}) \quad (14)$$

$$v_o'(t) = \frac{1}{2} \sum_{\omega_r = \omega_c, -\omega_c} \left(\sum_{i=-u}^{u} V_o'(\omega_r + i\omega_x) \cdot e^{j\beta_{\omega_r + i\omega_x}} \cdot e^{j(\omega_r + i\omega_x)t} \right) \quad (15)$$

where $V_o'(\omega_c + i\omega_x)$ and $\beta_{\omega_c + i\omega_x}$ represent the magnitude and phase respectively for each tone of $v_o'(t)$. Here again, $V_o'(-\omega_c - i\omega_x) = V_o'(\omega_c + i\omega_x)$, $\beta_{-\omega_c - i\omega_x} = -\beta_{\omega_c + i\omega_x}$ and j is the complex imaginary unit. u is related to the number of significant tones of interest present in the PA's output RF signal $v_o'(t)$, e.g. $u = 4$ in Fig. 4 since the number of tones is 9, ranging from $\omega_c - 4\omega_x$, $\omega_c - 3\omega_x \ldots 0 \ldots \omega_c + 3\omega_x$, $\omega_c + 4\omega_x$. (15) represents the system of equations that relates the PA's output IMD levels V_o' with the three-tone input RF signal V_{in} and the dynamic bias signal V_e for the 3-port PA representation proposed here.

The mathematical formulations of the proposed 3-port PA representation are now complete.

B. STEPS FOR EXTRACTING POLYNOMIALS G AND P
The following steps are followed to extract the coefficients of polynomials G and P. This sequence of steps may be used by the RFIC PA manufacturer at an advanced engineering phase of the development. The extracted coefficients may then be provided to a mobile equipment manufacturer as parameters of our proposed PA representation (represented by X in Fig. 1) that describe the typical behavior of the PA, and used for our proposed self-calibration (described with details in Section IV-D, Section VIII) embedded within the mobile unit.

Step 1: Using a three-tone V_{in} and with the PA's bias held at V_{dc}, the magnitude and phase of the output multi-tone signal V_o is measured. This measurement is repeated for a set of three-tone input signals that define the PA's input power range of interest. Using each of these V_o vs. V_{in} measurements in (3), a system of equations is now derived, the solution of which gives the coefficients a_1, a_3, a_5 etc. of the complex polynomial G.

Step 2: With the PA input excited with any one of the three-tone V_{in} values from Step 1, the PA's bias node is now excited with a multi-tone signal V_e i.e. its bias is now $V_{ctrl} = V_{dc} + V_e$. The magnitude of the power levels of the multi-tone signal V_o' at the PA's output is measured.

Step 3: Step 2 is now repeated for different values of the multi-tone dynamic bias signal V_e. The values of V_e chosen define the range of interest for the PA's dynamic bias signal. The PA's input three-tone signal V_{in} is held constant at the value used in Step 2. The corresponding PA output power levels for this set of V_e signal values are measured.

Step 4: With G already known from Step 1, the V_o' vs. V_e measurements of Step 2 and Step 3 are used in equations (12) to (15) to derive a new system of equations. The solution of this system of equations is the set of complex coefficients of the nonlinear polynomial P (p_{iql} as defined in (11)) that relates V_e with ΔV_a, and which translates into the PA's output signal V_o' under dynamic biasing.

The extraction of the PA representation is now complete.

Centering the range of the measurement values of Step 1, Step 2 and Step 3 significantly aids in solving the system of equations of Step 1 and Step 4. This is explained with

greater detail in Appendix A, as well as ways to handle the asymmetry of the PA's upper and lower IMD$_3$ levels.

IV. VALIDATION OF PROPOSED 3-PORT REPRESENTATION THROUGH COMPARISON WITH ADS^{TM} SIMULATION

A. DESCRIPTION OF SIMULATION TEST-BENCH

The formulations of the proposed representation are now validated through its benchmarking against an RFIC PA design within a simulation test-bench. The PA used is a 5GHz SOI CMOS PA in 0.18um technology from Tower-Jazz. It is a 3-stage design with a cascode structure and designed for flip-chip assembly on a 6 layer multi-chip module (MCM) further assembled on a PCB. Decoupling capacitors are present on all DC lines. The simulation software used is ADS^{TM} Dynamic Link^{TM}. All results shown for this design are performed using PEX^{TM} extracted views (for active devices) and post-layout simulations using the electromagnetic extraction tool EMX^{TM}. Design details of this PA are given in [12]. Its schematic is provided here in Section VII, Fig. 17. For the open-loop operation described in the present Section, resistance R_a in Fig 17 is kept open and the quiescent value of the PA's third stage gate bias is held at $V_{dc} = 0.355V$. Dynamic biasing is performed by externally applying an envelope signal V_e directly to the gate of the NMOS in the third stage (node g in Fig. 17 (a)) via 15nH inductors, using a baseband signal generator component in ADS^{TM}. The input excitation V_{in} is a three-tone RF signal with the two side-tones held 5dB lower than the center tone. The RF center frequency is $f_c = 5.4GHz$ and a spacing of $f_x = 50MHz$ is used.

B. PA LINEARIZATION THROUGH DYNAMIC GATE BIAS

With the PA's gate bias held at $V_{dc} = 0.355V$ and by varying V_{in} over the input power range of interest, the polynomial G given by (16) below is extracted. As shown in Fig. 5, an excellent match between the PA's simulated and predicted output tones is observed (less than 0.12dB error for the f_c-$2f_x$ tone, which itself is ~26dB below the f_c tone, at the characterization power level of 14dBm). A 5th-order polynomial is sufficient for G and unlike other PA representations (e.g. [18]), the coefficients remain unchanged over the power range of interest.

$$v_o(t) = (8.19 + j \cdot 1.48) \cdot v_{in}(t) + (-4.98 - j \cdot 1.56) \cdot v_{in}^3(t) + (3.40 + j \cdot 2.14) \cdot v_{in}^5(t) \quad (16)$$

The increase of the error at lower average output power levels does not affect the proposed representation's accuracy at 14dBm, since this error pertains to the G block only (not the P block). It will be shown in Section IV-C that the full representation (i.e. including both G and P blocks) accurately captures the PA's IMD performance over a significant range across the characterization power level.

With G extracted, a dynamic bias tone V_e at frequency f_x is added to the PA's DC bias. By varying the amplitude
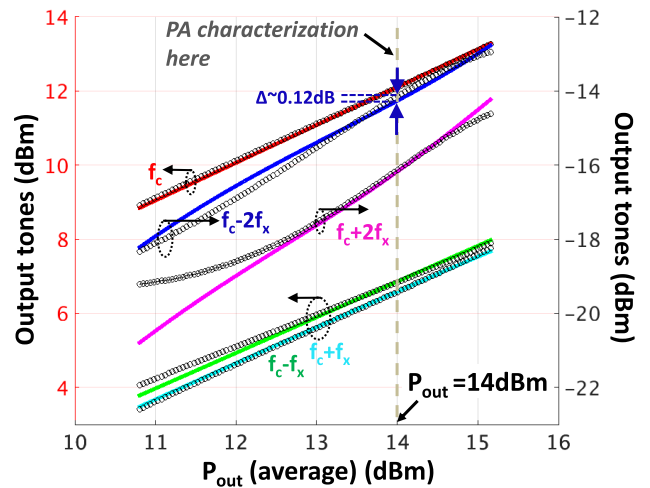

FIGURE 5. Simulated values (solid traces) and predicted values (circular marker traces) of the PA's output signal including the output tones at $f_c - 2f_x$ and $f_c + 2f_x$ which are due to the PA's nonlinearity under quiescent bias.

of V_e, noting the corresponding output multi-tone signals and solving the system of equations (12)-(15), the complex coefficients of the second-order polynomial P as represented in (11) are extracted and given by (17).

$$\Delta v_a(t)$$
$$= \frac{1}{2}(1.27 - j \cdot 0.07) \cdot v_e(t) \cdot cos(\omega_c t) + \frac{1}{2}(1.09 - j \cdot 0.31)$$
$$\cdot v_e(t) \cdot cos((\omega_c + \omega_x)t)$$
$$+ \left\{ \frac{1}{2}(0.56 - j \cdot 0.31) \cdot v_e(t) + \frac{1}{4}(-1.85 + j \cdot 0.12) \cdot v_e(t)^2 \right\}$$
$$\cdot cos((\omega_c + 2 \cdot \omega_x)t) + \frac{1}{2}(1.13 + j \cdot 0.12) \cdot v_e(t)$$
$$\cdot cos((\omega_c - \omega_x)t)$$
$$+ \left\{ \frac{1}{2}(0.69 + j \cdot 0.15) \cdot v_e(t) + \frac{1}{4}(-1.16 - j \cdot 0.50) \cdot v_e(t)^2 \right\}$$
$$\cdot cos((\omega_c - 2 \cdot \omega_x)t) \quad (17)$$

Fig. 6 shows a comparison of the PA's simulated IMD$_3$ with that predicted using our proposed 3-port representation as a function of V_e at the PA's characterization power level $P_{out} = 14dBm$. The proposed representation predicts with negligible error that setting V_e to 40mV, $\angle 0°$ yields a 4dB improvement in IMD$_3$. The 0° phase translates the fact that the delay through the driver stages and the bias interfacing (having minimal reactances) in the specific PA design of Fig. 17 is negligible for baseband signals. It is sufficient to truncate P to 2nd-order here, and the extracted P and G accurately captures the PA's performance over the range of interest of the PA's operating power and dynamic bias levels. Note that experimental results shown in Section V will demonstrate a comparable IMD$_3$ improvement of ~4dB, using our proposed representation and starting from experimental measurements. A comparison of the simulated and predicted time domain form of the PA's output envelope signal with $V_e = 40mV$
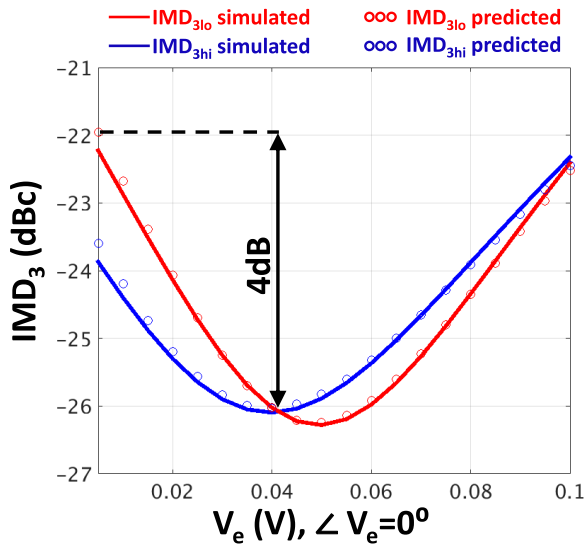
FIGURE 6. Simulated values (solid traces) and predicted values (circular marker traces) of the PA's output IMD$_3$ under dynamic bias at P$_{out}$(avg)=14dBm.
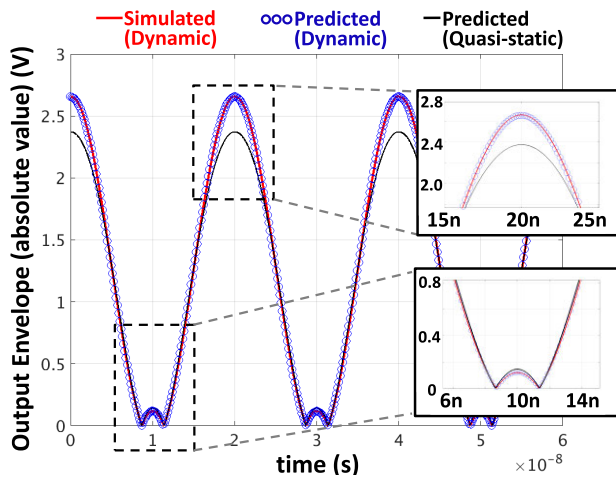

FIGURE 7. Simulated and predicted time domain form of the PA's output envelope signal under dynamic bias. The time domain form predicted using only the quasi-static representation is also shown.

in Fig. 7 further highlights the accuracy of the proposed 3-port PA representation.

C. APPLICATION EXAMPLE 1: FEED-FORWARD DYNAMIC BIASING FOR OPTIMIZING PA LINEARITY

We now demonstrate an application, illustrated in Fig. 8, where the $v_{in}(t) - v_o(t) - v_e(t)$ multi-tone relationships (16) and (17) of the extracted 3-port PA representation X is used to build a pre-distortion function F embedded as a signal processing element within the baseband chipset of a transmitter front-end. Note that the baseband processor also generates Env_{in}, which is the envelope signal of the PA's input modulated signal V_{in}. The parameters of X may
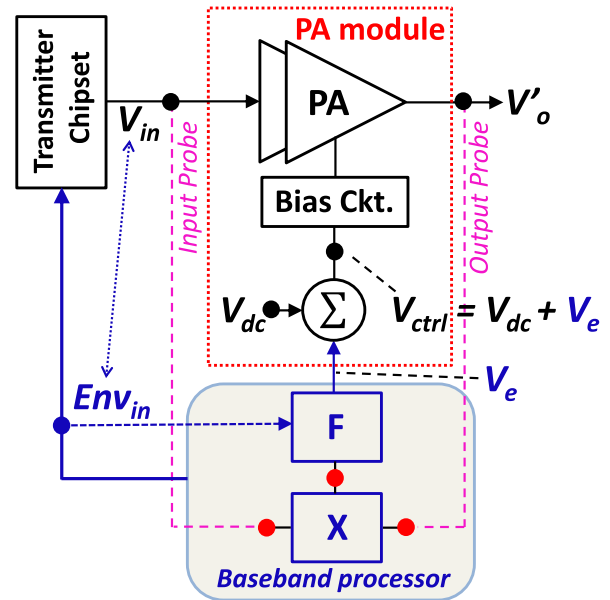

FIGURE 8. Implementation of feed-forward dynamic biasing embedded within mobile unit for linearization of PA. *F* is extracted using our 3-port representation *X* of the PA module, and applied to the PA module to optimize its output linearity.

be provided by the PA manufacturer in a real implementation. The function F is aimed at performing the necessary embedded adjustment (performed within the mobile unit) on V_e to minimize the PA's output IMD$_3$ through feed-forward dynamic biasing. F therefore gives the relationship between the PA's input envelope Env_{in} and its bias signal V_e that allows achieving optimum PA output linearity. In this example, F is determined using MATLAB^{TM} starting from the same 3-port representation X used for Fig. 6 and that was characterized at P$_{out}$ = 14dBm.

Note that though F is extracted using our proposed 3-port representation X, the PA's improved performance using the F block that is shown next is evaluated by applying F (defined using the frequency-domain defined device FDD functional block in ADS^{TM}) to the 5GHz SOI CMOS PA design itself (represented by 'PA module' in Fig. 8) within the ADS^{TM} circuit simulation environment, and not by merely applying F to the extracted 3-port representation X of this PA module.

Fig. 9 shows the PA's output IMD$_3$ vs P$_{out}$ without and with the feed-forward dynamic biasing (using the F processing block) applied to the PA schematic. The value of the IMD$_3$ at the characterization power level P$_{out}$ = 14dBm in Fig. 9 is −26dBc, which is identical to the optimum improved IMD$_3$ value given in Fig. 6 (also simulated at P$_{out}$ = 14dBm) and which was obtained by externally applying a dynamic biasing signal V_e. The exact match of the improved IMD$_3$ value in Fig. 6 and Fig. 9 at the characterization power level of the 3-port PA representation clearly validates the accuracy and usefulness of the proposed 3-port representation for implementing the embedded feed-forward dynamic biasing aimed at PA linearization as shown in Fig. 8.
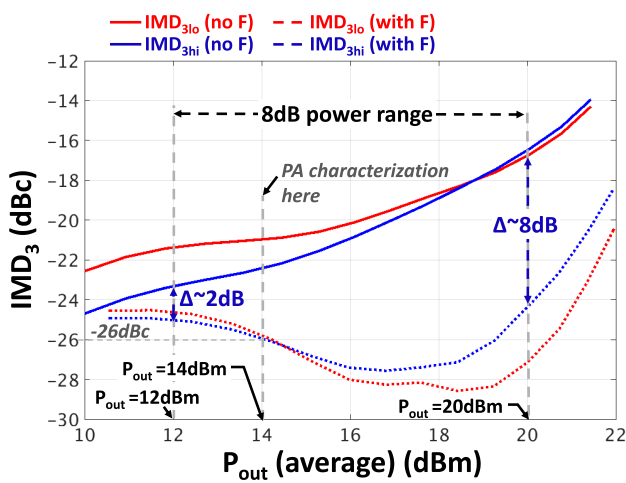
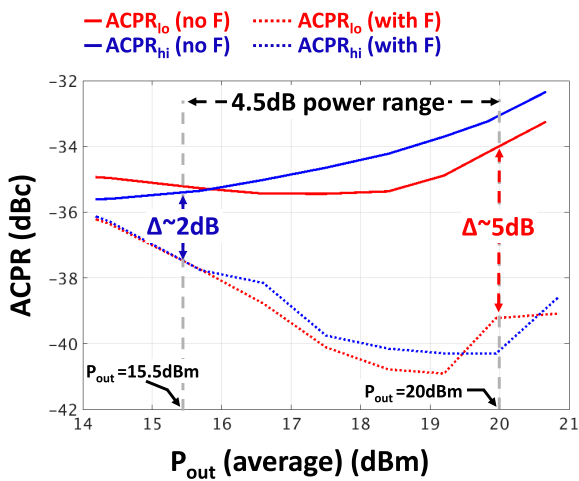FIGURE 9. PA's simulated output IMD$_3$ vs. P$_{out}$ without and with *F*.

FIGURE 10. PA's simulated output ACPR vs. P$_{out}$ without and with *F*.

The PA's P$_{out}$ values for which using *F* achieves significant IMD$_3$ improvement (2dB to 8dB improvement) ranges from its maximum output power (P$_{out}$ ~20dBm) and up to 8dB back-off (P$_{out}$ ~12dBm). It may be observed that this 8dB power range for which significant IMD$_3$ improvement is achieved using *F* is shifted slightly towards the higher range of PA output power levels with respect to P$_{out}$ = 14dBm, the characterization power level of *X*. A similar shift is also observed in the power range where PA linearity is improved when it is excited with a modulated signal (Fig. 10), and will be explained in the succeeding paragraphs.

The same PA schematic is now excited using a modulated signal in ADS^{TM} and its output linearity, calculated using ACP Reduction (ACPR) values, is measured without and with the *F* block applied to it. The excitation used is an RF carrier modulated by a Forward Link CDMA signal with a signal bit rate of 1.2288MHz, with 4 samples/bit and 256 total number of symbols. It is generated using the *PtRF_CDMA_IS95_FWD* component in the

Sources-Modulated library in ADS^{TM}. The *F* block itself remains unchanged from the preceding discussion and is not determined using a modulated signal; as described earlier, *F* is determined using *X* derived using multi-tone signals and characterized at P$_{out}$ = 14dBm. The PA's input modulated signal is processed by this computed *F* block.

As shown in Fig. 10, an ACPR improvement of ~2dB to ~5dB is achieved for output power levels ranging from its maximum output power (P$_{out}$ ~20dBm) to P$_{out}$ ~15.5dBm. The modulated output signal centered at the RF carrier frequency for P$_{out}$(average) =18.3dBm is also shown in Fig. 11, and clearly demonstrates the linearization that is achieved using the *F* block.
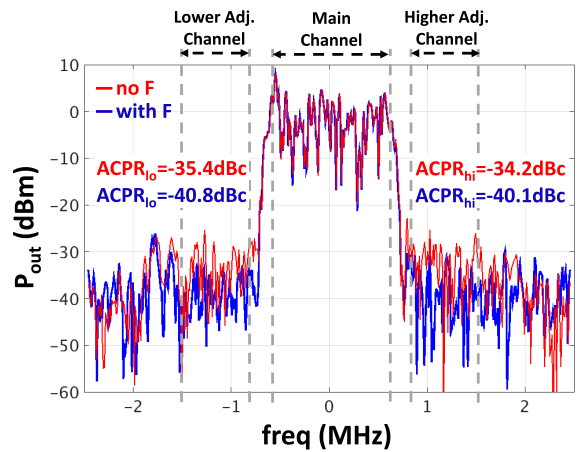

FIGURE 11. PA's simulated output signal (centered at carrier frequency) under modulated excitation at P$_{out}$(avg)~18.3dBm, without and with the *F* block.

The significant improvement in the PA's linearity at higher output power levels compared to the improvement at the PA characterization power P$_{out}$ = 14dBm as observed in Fig. 9 and Fig. 10 is specific to this PA design and its nonlinear characteristics. The increased level of nonlinearity at these higher power levels for this specific PA design causes a heightened linearizing effect, dependent also on the specific pre-distortion function *F* implemented, as per Fig. 8. This results in the observed IMD$_3$ and ACPR improvement for the higher range of output power levels. Such an improved linearity may be attributed to the phenomenon of *sweet spots* [29], [30] that is well known among PA designers, and which the proposed pre-distortion in Fig. 8 facilitates achieving for this specific PA design at power levels close to its maximum power. It is also worthwhile to note that there is a ~3.5dB shift in the output power levels where significant ACPR improvement is achieved with a modulated signal (starting at P$_{out}$ ~15.5dBm), when compared to the power levels where significant IMD$_3$ improvement is achieved with a multi-tone signal (starting at P$_{out}$ ~12dBm). This shift stems from the difference between the PA's nonlinear behavior that is captured during characterization with a 3-tone (sine wave) ~6dB peak-to-average envelope variation, and the PA's resulting nonlinear behavior due to the CDMA envelope pattern (of the

modulated signal) with a ~7.5dB peak-to-average envelope variation. Such a shift, however, may be compensated for by computing F based on our proposed 3-port PA representation X characterized at different output power levels, and which allows ensuring optimum PA linearity in the power range of interest where ACPR improvement is sought.

Therefore, the above results demonstrate the pertinence of our proposed PA representation derived from a 3-tone characterization in the context of embedded adjustment of the applied dynamic biasing within the mobile unit, for linearity improvement under modulated excitation.

D. APPLICATION EXAMPLE 2: USE OF PROPOSED PA REPRESENTATION FOR PERFORMANCE COMPENSATION WITHIN EMBEDDED SELF-CALIBRATION AGAINST PART-TO-PART VARIATIONS

A second application example is now presented where the proposed 3-port PA representation X extracted in Section IV-B is used to predict the embedded pre-distortion F necessary for linearity optimization of a new PA. This new PA exhibits some level of performance variation with respect to the original PA that was characterized and linearized in Section IV, sub-sections B-C, and the degree of this performance variation shown here may be typically expected from one PA part to another within different mobile equipment. We demonstrate that by using an adjusted version of the original X, to compute an adjusted value of the pre-distortion F that is then applied to the new PA as part of the embedded optimization within the mobile unit shown in Fig. 8, enables a significant improvement of the new PA's linearity. This adjustment, performed using quasi-static measurements alone of the new PA's input and output power, accounts for the performance variation of the new PA with respect to the original PA, and the simple probing circuitry shown in Fig. 8 that is necessary for these measurements makes it suitable for implementation in embedded self-calibration applications within the mobile communication equipment (Fig.1).

As noted in Section IV-C, the parameters of the 3-port representation X that describe the original PA may be extracted by the PA manufacturer during an advanced engineering phase, and provided to the mobile equipment manufacturer. The automatic embedded adjustment (within the mobile equipment) of these original X parameters, to account for part-to-part PA performance variation, is what we refer to as our proposed embedded self-calibration.

For our demonstration here, the PA performance variation is introduced by changing the bias of the original PA, to force a change of 0.9dB in the output referred P_{1dB} (PA1 in Fig. 12). In an actual implementation, a measurement of the *ratio* between the outputs of the same simple probing circuitry at the PA's input and output (Fig. 8) should allow detecting such part-to-part variations in the PA's compression with respect to an original PA specification. Table 1 shows PA1's IMD_{3hi} values under constant DC bias obtained using simulation of the PA1 schematic in ADS^{TM} for an output power range
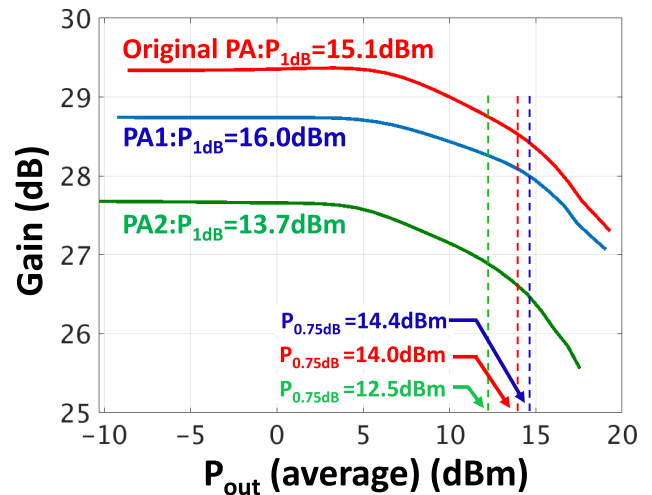

FIGURE 12. Comparison of Gain vs. P_{out} profile for the original PA and the new PA examples of Table 1 and Table 2.

TABLE 1. Simulated vs predicted values of optimum dynamic bias for PA1.

P_{out} (average) of PA1 (dBm)	14.0	14.2	14.4	14.6	14.8
Values under constant (DC) bias					
IMD_{3hi} (dBc)	-22.84	-22.75	-22.70	-22.58	-22.50
Values from pre-distortion predicted using Adjusted 3-port PA Representation (G only)					
Dynamic Bias — Value (mV)	37.6	38.5	39.8	40.5	42.0
IMD_{3hi} — Value (dBc)	-24.86	-25.10	-25.35	-25.60	-25.80
IMD_{3hi} — Δ (dB)	2.02	2.35	2.65	3.02	3.30

of 0.8dB around P_{out} = 14.4dBm. IMD_{3lo} values are not shown to keep Table 1 concise. P_{out} = 14.4dBm is chosen for our analysis since it is the output power level where the gain of PA1 has compressed by ~0.75dB (hereafter referred to as $P_{0.75dB}$), and X for the original PA was extracted at P_{out} = 14.0dBm in Section IV-B, which is also the $P_{0.75dB}$ for the original PA. This $P_{0.75dB}$ point is expected to be in the lower range of power levels where linearization through pre-distortion using F is effective, as observed in Fig. 9.

We now proceed with adjusting the original 3-port PA representation X, to account for the performance variation of PA1 compared to the original PA, to be used for predicting the adjusted pre-distortion F necessary to optimize PA1's linearity. For this, it is only required to adjust the coefficients of polynomial G (i.e. a_1, a_3 and a_5 within X in Fig. 8) starting from their original values provided by the PA manufacturer, by *measurement of the amplitudes only* of PA1's input three tones and the output three tones (i.e. at frequencies $f_c - f_x$, f_c and $f_c + f_x$) and only at the power level of interest (i.e. at P_{out} = 14.4dBm). In an actual implementation, this would be done through the input-output probes in Fig. 8, over the

TABLE 2. Simulated vs predicted values of optimum dynamic bias for PA2.

P_{out} (average) of PA2 (dBm)	12.1	12.3	12.5	12.7	12.9
Values under constant (DC) bias					
IMD$_{3hi}$ (dBc)	-23.25	-23.15	-23.00	-22.90	-22.75
Values from pre-distortion predicted using Adjusted 3-port PA Representation (G only)					
Dynamic Bias — Value (mV)	30.8	31.7	32.5	33.4	34.2
IMD$_{3hi}$ — Value (dBc)	-27.75	-28.00	-28.25	-28.50	-28.80
IMD$_{3hi}$ — Δ (dB)	4.50	4.85	5.25	5.60	6.05

narrow power range of envelope variation of the 3-tone signal. This requires only simple envelope detector circuitry. Such simplicity holds promise for its use in embedded self-calibration applications that are based on incorporating the calibration set-up within the mobile equipment.

The optimum dynamic bias values predicted by pre-distortion through the adjusted F computed using this adjusted 3-port PA representation are also shown in Table 1 (in blue). IMD$_3$ improvement Δ of 2.02dB to 3.30dB over the constant bias case is possible for the targeted power range when using these predicted dynamic bias values, and represents a significant improvement in PA1's linearity. This demonstrates the effectiveness of the set-up embedded within the mobile unit (Fig.8) for our proposed embedded self-calibration. The difference in the IMD$_3$ improvement at its $P_{0.75dB}$ power level between the original PA ($\sim$4dB at P_{out} = 14dBm, Fig. 9) and PA1 (2.65dB at P_{out} = 14.4dBm, Table 1) is a result of the two PAs operating with different bias conditions, which translates into the applied pre-distortion having a different degree of linearizing effect.

A more drastic change in the PA's performance is now considered by forcing a change of 1.4dB in the PA's output referred P_{1dB} (PA2 in Fig. 12). This time, both the bias and the output matching network are changed. The comparison of IMD$_3$ levels of PA2 with or without pre-distortion through F is again made at the $P_{0.75dB}$ output power level (12.5dBm for PA2) and is shown in Table 2. It can be seen that the IMD$_3$ levels are significantly improved (by more than 5dB) compared to the constant bias case, by pre-distortion using the adjusted X to account for the performance variation of PA2 compared to the original PA. The higher levels of IMD$_3$ improvement for PA2 in Table 2 compared to PA1 in Table 1 may be attributed to PA2 operating under stronger nonlinearities, given the change in both the bias and the output matching network for PA2, and the heightened linearization effect due to the sweet-spot phenomenon.

Note that the resulting improvement in IMD$_3$ through pre-distortion in Tables 1-2 is function of the assumption of updating the G coefficients only, and using very simple probe circuitry. We restrict our analysis in this paper to the use of such simple probes only, within an embedded self-calibration

set-up in the mobile unit. However, simulations show that by additionally adjusting the coefficients of P in X allows even further improvement of the IMD$_3$ levels. This suggests an interesting possibility of using our proposed PA representation to further optimize PA linearity while accounting for part-to-part variation. It would require a one-time measurement followed by adjustment, based on computation using the proposed 3-port representation. A potential approach to accomplish this is to use more precise envelope detectors in the probing circuitry, but over a narrow power range only, for the measurement of two additional output tones (at intermodulation frequencies $f_c - 2f_x$ and $f_c + 2f_x$) for the new PA, therefore allowing an adjustment of the P polynomial coefficients. The G coefficients may be left to the earlier values obtained through the 3-tone quasi-static measurements. This measurement of the two additional output tones is performed with a 1-tone dynamic bias signal at frequency f_x applied to the PA's bias node. It can be performed from one mobile equipment to another, and it is sufficient to perform the measurement at the rated power only.

V. EXPERIMENTAL VALIDATION
A. POWER AMPLIFIER AND DEVICE TECHNOLOGY
For experimental validation of the proposed 3-port PA representation, we use the SE5003 WiFi PA from Skyworks Solutions, Inc., but modified by Skyworks to allow access to the internal biasing circuitry specifically for our tests. This enables the application of an envelope-dependent dynamic bias signal to the second and/or third PA stages. The PA is fabricated using Indium Gallium Phosphide (InGaP) Heterojunction Bipolar Transistor (HBT) technology. It is capable of better than 3% EVM at 25dBm output power (802.11a signals) from 5.15GHz to 5.9GHz, has a P_{1dB} of about 32dBm and a gain of about 32dB [31].

B. TEST SET-UP
Fig. 13 shows the test set-up schematic of the PA dynamic biasing experiment. The RF and Baseband Generator is used to synthesize the RF and the baseband signals applied to the input node (port *1*) and bias node (port *3*) respectively. The spectral content at nodes *1*, *2* and *3* are measured with spectrum analyzers, while power measurements at nodes *1* and *2* are done using a power meter.

An important requirement for the testbench in Fig. 13 is that the phase of the baseband multi-tone signal at port *3* be precisely known, calibrated and controlled to extract *phase-coherent* relationships between the signals at ports *1*, *2* and *3*, in addition to allowing their precise amplitude control. While amplitude control is easily achieved, phase control must be achieved such that at any instant of time, the phase at nodes *1*, *2* and *3* are calibrated using a single time reference. The RF and Baseband Generator achieves this using the oscilloscope measurements of the signals at ports *1*, *2* and *3* (shown by blue dotted arrows in Fig. 13) together with MATLAB^{TM} algorithms running on the computer that controls the
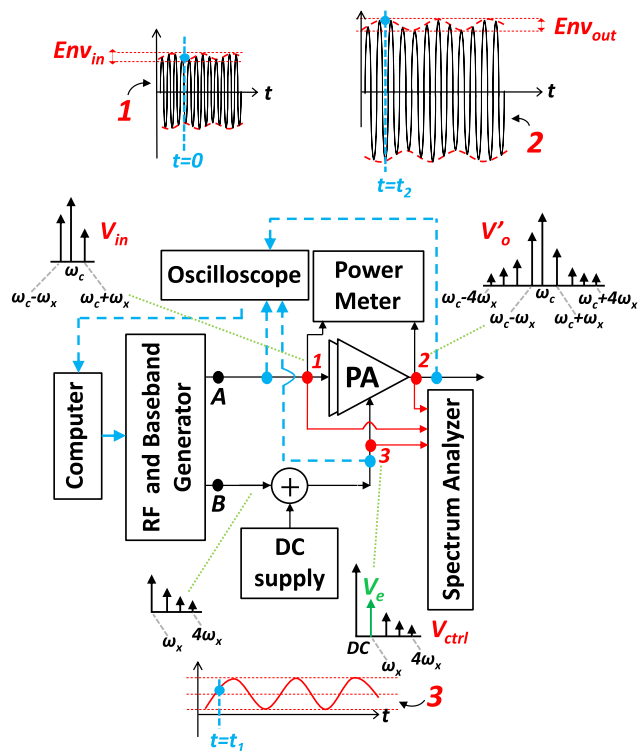
FIGURE 13. Test set-up for experimental validation of proposed 3-port PA representation.

FIGURE 14. Photograph of experimental test set-up shown in Fig. 13. A photograph of the SE5003 PA test-board (DUT) is also shown.

FIGURE 15. Measured values (dotted markers) and predicted values (solid traces) of the PA's IMD$_3$ under dynamic bias V_e. V_e is the V_{ctrl} tone at ω_x with the phase kept constant at 80°. Other tones are present in V_{ctrl} but are not varied. The PA's P$_{out}$(average) is 29.2dBm.

equipment. This enables adjusting the phase at nodes *1, 2* and *3* with respect to one single time reference.

C. MEASUREMENTS AND VALIDATION

The procedure detailed in Section III-B to extract the proposed 3-port PA representation is now applied to the SE5003 WiFi GaAs HBT PA using a 3-tone RF signal with a frequency spacing of 1.5MHz (i.e. total signal bandwidth of 3MHz) and for P$_{out}$(average)=29.2dBm. The PA is therefore being operated in the vicinity of its maximum rated linear output power (P$_{1dB}$ ~32dBm). The representation is characterized with the multi-tone dynamic bias signal V_{ctrl} applied to the HBT base in the PA's third stage, since it is observed to have a greater effect on the linearity than applying it to the second stage. The extracted representation is similar in form to (16)-(17) but with different coefficients, and is not shown here for conciseness.

Note, however, that a third-order *P* polynomial is necessary to accurately capture the PA's nonlinearity under dynamic biasing for the experimental validation here. This increase in order of *P* accounts for the larger nonlinearities associated with the particular HBT PA design used here compared to the CMOS PA discussed in Section IV.

With the extraction of the proposed 3-port PA representation complete, it is now used to predict the necessary pre-distortion through dynamic bias, i.e. the necessary V_{ctrl} signal in Fig. 13, to linearize the DUT at the characterized power
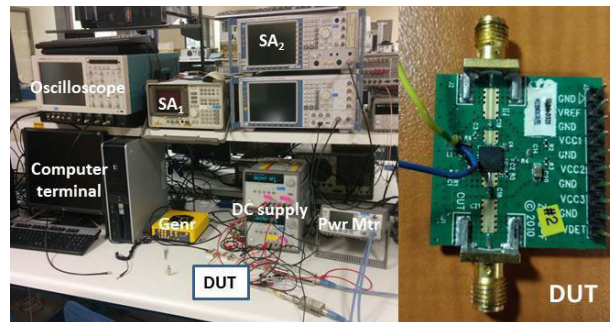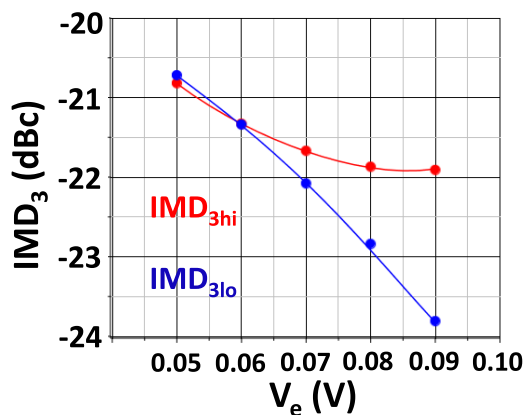
level. Because the variation of the tone V_e (at frequency ω_x) in V_{ctrl} has the greatest impact on PA linearity, the plots in the discussion that follows shows the variation of the output IMD$_3$ with the magnitude and phase of this V_e tone only, even though higher frequency tones (at $2\omega_x$, $3\omega_x$, $4\omega_x$) are present in V_{ctrl} during both PA characterization and in the test-cases described next.

As shown in Fig. 15, the proposed PA representation allows accurately predicting the pre-distortion through the dynamic bias tone V_e required to improve the IMD$_3$ by up to 3dB, using amplitude control only of the V_e tone. Further IMD$_3$ improvement is also possible by additionally varying the phase of the V_e tone. As shown in Fig. 16, the proposed 3-port representation allows accurately predicting the amplitude and phase (0.09V, ∠100°) of V_e that is necessary to achieve more than 4dB of IMD$_3$ linearization.

VI. COMPARISON WITH MODIFIED VOLTERRA SERIES

Of the recent advances in analytical PA representations, [18] describes a 3-port Volterra-based representation for supply-modulated RF PAs, derived with a 2-tone excitation. Because of its apparent similarity to our proposed 3-port representation, it is useful to discuss the significant differences between
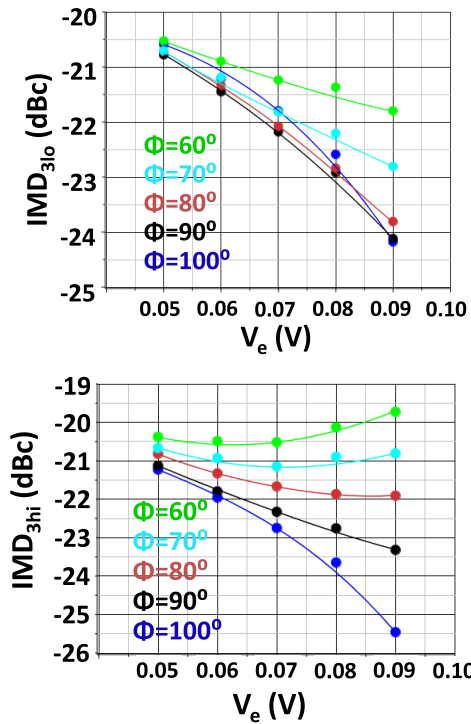
FIGURE 16. Measured values (dotted markers) and predicted values (solid traces) of the PA's IMD$_3$ under phase variation in addition to amplitude variation of its dynamic bias, at P$_{out}$(average)=29.2dBm.

In contrast, it was shown in Section IV that with our proposed representation, a relatively small number of coefficients (of G and P) require being stored. These are extracted (and adjusted) using a simple training sequence based on a minimum number of relatively simple measurements performed using a low-complexity probing circuitry, and successfully answers the requirements of our embedded self-calibration application within mobile equipment.

It was also shown in Fig. 6 that our proposed 3-port PA representation allows predicting with negligible error an improved IMD$_3$ of −26dBc via pre-distortion for the SOI CMOS PA in Section IV. Similarly, the experimental values in Fig. 16 shows that our proposed representation accurately captures the nonlinearities and allows the prediction of the pre-distortion necessary to achieve an improved IMD$_3$ of less than −25dBc for an industry-designed GaAs PA. The error in prediction of the IMD$_3$ for this GaAs PA using our proposed representation is negligible (< 0.1dB, Fig. 16) when the PA is tested at power levels in the vicinity of its P$_{1dB}$ (i.e. when PA nonlinearity is significant). These error values are comparable to those associated with using the Volterra-based PA representation in [18] for predicting output IMD$_3$ levels, while operating the PA under similar degrees of nonlinearity and comparable IMD$_3$ under dynamic conditions (IMD$_3 \sim$ −25dBc in [18, Fig. 9(a)]). Therefore, our proposed 3-port PA representation allows accurately capturing PA nonlinear behavior that is of the same degree as that discussed in [18], but without the significantly more complex training sequences associated with extracting Volterra kernels.

Additionally, it has been shown in Section V-C that it was necessary to increase the order of P from two to three in order to capture with minimal error (<0.1dB) the effect of the dynamic biasing signal on a GaAs HBT PA's nonlinearity, when the PA is operating in a significantly nonlinear region (P$_{out}$ $\sim$29.2dBm). Increasing to the third-order the kernels in (2) for the Volterra-based representation in [18] has not been demonstrated, nor the accompanied complexity that would ensue for such higher-order Volterra characterization, given the considerable challenges associated even with the extraction of first-order Volterra kernels [21].

the two approaches in terms of their intended application, the advantages and the disadvantages.

Reference [18] uses a first-order truncation of the full Volterra series in order to reduce the complexity of extracting the higher-order kernels. The first-order kernel values in [18] are shown to vary as a function of three variables - the RF Input Power, the DC supply and the modulation signal bandwidth [18, Figs. 5–7]. Since the kernels are derived for a large range of these three variables, they remove the necessity for real-time coefficient updates that may be associated with tuned PA representations [18, p. 9, Paragraph 1], tuned PA representations according to [18] being those that are valid only when used under identical operating conditions as during characterization. This is an interesting feature of the PA representation in [18]. On the other hand, such a large number of kernel values require being stored in some form (for example, as look-up tables) which allows them to be structured as *nonlinear filters which nonlinearly change versus time* [18, p. 6]. Dynamically addressing and updating look-up tables which are functions of three separate variables (the RF Input Power, the DC supply and the modulation signal bandwidth), as part of a training sequence, makes it too complex for use in our proposed context of embedded self-calibration within mobile equipment to account for part-to-part variations (Fig. 1). This is because of the complexity of the probing interfacing and training sequence that would be required to implement a dynamic updating of the look-up table that is a function of these three separate variables.

VII. APPLICATION TO CLOSED-LOOP PA WITH EXPERIMENTAL VERIFICATION

Closed-loop PA architectures relying on feedback have been widely demonstrated to improve PA performances. For example, [13] improves PA linearity by using negative feedback through active elements for gain compensation when the PA's compression is significant. References [14] and [15] use negative feedback in VGA architecture to regulate the system's overall gain. Our proposed 3-port PA representation is useful for both PAs and VGAs under closed-loop operation, using either negative or positive feedback.

In this section, its usefulness is highlighted by applying it to the recently proposed positive envelope feedback linearization scheme, where the PA's output envelope signal is applied in positive feedback to the bias node [12], [32], [33]. To the
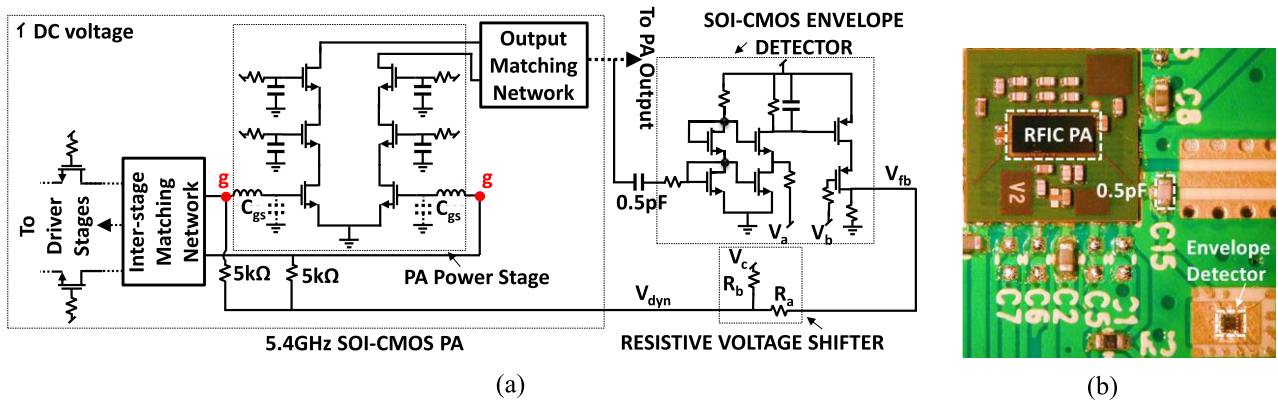
FIGURE 17. (a) Simplified schematic showing closed-loop PA using positive envelope feedback (b) Prototype system with PA and Envelope Detector [12].

best of the authors' knowledge, for the first time, an analytical approach using a 3-port representation is used to predict the conditions for closed-loop stability in an envelope feedback system as well as the design requirements of the feedback elements for optimum linearity, without relying solely on trial and error.

While this is demonstrated here in the context of positive envelope feedback through sub-sections A-E, the proposed PA representation may also be used for closed-loop PAs within an embedded self-calibration set-up in the mobile unit (such as the set-up in Fig. 1) to verify PA stability as well as optimize linearity. This is discussed in Section VIII.

A. DESCRIPTION OF DEVICE UNDER TEST

The device under test (DUT) is shown in Fig. 17 [12]. Both simulation results of the PA schematic (Fig. 17(a)) and measurements on the prototype (Fig. 17(b)) are referred to here. The 5.4GHz PA and the envelope detector are fabricated using SOI-CMOS 0.18um technology from TowerJazz. The three-stage flip-chip PA is interfaced to the PCB via a 6 layer MCM. The reader may refer to [12], [32], [33] for further details.
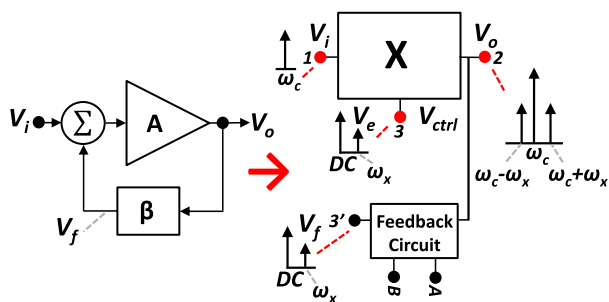

FIGURE 18. Closed-loop PA under positive feedback, and equivalent open-loop form using proposed 3-port PA representation.

Fig. 18 gives a schematic representation of the closed-loop PA using positive envelope feedback on the left, and converts it into an open loop system using our proposed 3-port PA representation (indicated by X) on the right. The feedback

circuit in Fig. 18 is the high input impedance system composed of an envelope detector and a voltage shifter as shown in Fig. 17 and detailed in [12]. Two parameters critical to the implementation shown in Fig. 17 are the threshold and the slope of the detector used in the feedback circuit. The underlying circuit operation and characteristics are described in [12, Fig. 5]. The values of these two parameters are voltage-controlled, represented by signals A and B in Fig. 14. Signal A corresponds to signal V_a in Fig. 17, which sets a threshold at the source of an NMOS comparator. Signal B corresponds to signal V_b in Fig. 17, which controls the gain of an output PMOS stage.

X is first extracted using the procedure given in Section III-B. At the end of this extraction procedure, the coefficients of complex polynomials G and P that constitute X in Fig. 18 are known for power levels where the PA is under gain compression, and where the application of positive envelope feedback is effective at improving PA performance. The extracted representation is similar in form to (16)-(17), and is not shown here for conciseness.

B. EXPRESSION FOR CONVERSION GAIN

For determining the expression of loop stability, the PA's conversion gain (C) from the dynamic bias signal at node V_{ctrl} to the output envelope signal at node V_o in Fig. 18 is first calculated. For this, the 3-port PA representation (X in Fig. 18) is excited using a single baseband tone of amplitude V_e (at frequency ω_x) at the bias node, a single RF tone of amplitude V_i at the input node and measuring the amplitude of the resulting output multi-tone signal V_o. The value of V_i is chosen such that the PA is operating under gain compression. For V_o, the measurement of amplitudes alone and limited to that of the three primary tones (i.e. at frequencies $\omega_c - \omega_x$, ω_c and $\omega_c + \omega_x$) is sufficient, given that the IMD$_3$ tones have a negligible contribution to the conversion gain. With the help of the formulations in Section III-A, the PA's conversion gain (C), when the input excitation is V_i and bias tone is V_e, is given by (18). Its detailed derivation is given in Appendix B.

$$C(V_i, V_e) = a_1 \cdot p_{111} + a_1 \cdot p_{112} \cdot V_e + a_3 \cdot f_1(V_i)$$
$$+ a_3 \cdot f_2(V_e) + a_3 \cdot f_3(V_i, V_e) \quad (18)$$

C. FEEDBACK CIRCUIT TRANSFER FUNCTION

A mapping of the feedback circuit's transfer function (from RF input V_o to baseband output V_f) as a function of A and B is now performed. For this mapping, the input of the feedback block is excited with the same multi-tone signal V_o as in Section VII-B. Leaving the feedback circuit connected to the PA output ensures that the feedback circuit's transfer function is evaluated with the right input conditions, while also ensuring the correct load conditions at the PA's output. For a particular value of A and B, the transfer function of the feedback block is given by (19).

$$\frac{V_f(\omega_x)}{Env(V_o)} = f(A, B) \quad (19)$$

where $V_f(\omega_x)$ is the amplitude value of V_f at the frequency ω_x and $Env(V_o)$, also at frequency ω_x, refers to the envelope of the PA's modulated output RF signal V_o. By repeating the measurement given by (19) for various values of A and B, the mapping of the feedback circuit's transfer function is generated and stored as a look-up table.

D. CONDITIONS FOR LOOP STABILITY

The conditions for stability of the closed-loop system in Fig. 18 is based on the well-known Barkhausen gain margin and phase margin stability criteria. However, only the gain margin is considered since the positive feedback necessarily introduces a $\sim 360°$ phase shift across the PA bandwidth. Hence it leaves no possibility of phase margin design. Accordingly, the condition for stability is given by (20).

$$C(V_i, V_e) \cdot f(A, B) < 1$$

i.e.

$$f(A, B) < \frac{1}{a_1 \cdot p_{111} + a_1 \cdot p_{112} \cdot V_e + a_3 \cdot f_1(V_i) + \dots}$$
$$(20)$$

(20) is the condition for stability of the closed-loop circuit using positive envelope feedback at the input power level corresponding to V_i and bias tone V_e. By calculating $C(V_i, V_e)$ for a few more V_i levels that define the PA's power levels where positive envelope feedback is of interest, the condition to maintain closed-loop stability at these power levels is also determined. For each such calculation, V_i is kept constant while V_e is considered a small-signal input. The conversion gain $C(V_i, V_e)$ given by (18) is the value of the PA's output envelope over V_e. The look-up table of Section VII-C is then used to determine the values of A and B that satisfy (20) for these calculated values of $C(V_i, V_e)$ at different power levels, and therefore the conditions to ensure the closed-loop PA's stability are known.

(18), (19) and (20) are now used to determine the limit value for the conversion gain to ensure stability of the closed-loop PA shown in Fig 17. Its computed value is

expressed in (21), and the limit condition on the feedback circuit transfer function to ensure stability by (22).

$$C(V_i, V_e) = |a_1 \cdot p_{111} + a_1 \cdot p_{112} \cdot V_e + \dots| = 4.71 \, {}^V\!/_V$$
$$\text{i.e. } C(V_i, V_e) = 13.46 dB \quad (21)$$
$$f(A, B) < {}^1\!/_{4.71} = 0.21 \text{ i.e. } -13.46 dB \quad (22)$$

(21) gives the value of $C(V_i, V_e)$ when the PA is operating close to approximately the lowest power level from where the application of positive envelope feedback becomes useful. This corresponds to the power level when the PA starts compressing. The PA's gain drops for higher power levels, and consquently its conversion gain from the bias node V_{ctrl} to the RF node V_o also drops. Hence, the value of $f(A, B)$ given by (22) represents the critical limiting value to ensure closed-loop stability. For higher power levels, the value of $f(A, B)$ may be higher without compromising the closed loop PA's stability.

In comparison, simulation of the circuit in Fig. 17(a) with ADS$^{\text{TM}}$ gives a conversion gain of 13.1dB, which shows that the value (21) predicted using the proposed 3-port PA representation is quite accurate. The small error between the two values is due to the approximation based on using a 1-tone RF signal V_i to derive (18) (Fig. 18), while the coefficients a_1, a_3 and a_5 were derived using a 3-tone RF signal V_i. (22) translates into the limits on A and B given by (23) for this particular design. Their actual values are set with an adequate safety margin to guarantee stable behavior of the PA with positive envelope feedback.

$$\text{Control signal for detector threshold} : A > \sim 2.0V$$
$$\text{Control signal for detector slope} : B > \sim 1.1V \quad (23)$$

E. ADJUSTMENT OF DETECTOR PROFILE FOR LINEARITY IMPROVEMENT OF PA

With the 3-port representation parameters and the limiting values of A and B that ensures the closed-loop PA's stability known, the following steps are followed to determine the values of A_{opt} and B_{opt} within this range that optimizes the positive envelope feedback PA's linearity:

Step 1: The 3-port PA representation is used to determine the values of the dynamic bias tone V_e at frequency ω_x required to optimize the open-loop PA's IMD$_3$ under a 3-tone RF excitation V_i, for values of output power P_{out} that lie in the range where positive envelope feedback is useful i.e. where the PA gain is under compression.

Step 2: The look-up table obtained in Section VII-C is used to determine a single combination of A and B, called A_{opt} and B_{opt}, which satisfy the following. First, A_{opt} and B_{opt} must satisfy the stability (20). Second, A and B are adjusted to A_{opt} and B_{opt} such that it allows matching the output of the feedback circuit V_f (at frequency ω_x) to the already computed optimum bias values V_e (also at frequency ω_x) of Step 1, at the corresponding values of P_{out}.

With A_{opt} and B_{opt} set accordingly, the loop is now closed. The resulting closed-loop PA with positive envelope feedback has an improved gain profile which translates into close to optimum linearity, while ensuring PA stability.

By applying Step 1 and Step 2 to the PA design of Fig. 17, A_{opt} and B_{opt} were found to be 2.6V and 1.6V respectively. Closing the positive envelope feedback loop with A and B set to these values, the measured values of the closed-loop PA's adjusted CW gain is shown in Fig. 19. The corresponding values of the dynamic bias signal V_{dyn} is also shown. The resulting gain flatness over the output power range from 16dBm to 21dBm as illustrated in Fig. 19 is achieved while also guaranteeing closed-loop PA stability, and translates into a linearity improvement as shown in [12, Fig. 7].
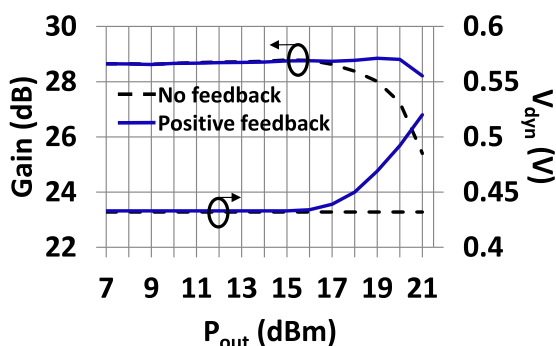
In Section IV-C, the use of these parameters for extracting a pre-distortion function F aimed at PA linearization is shown. In Section IV-D, a method of self-calibrating this pre-distortion function F, to account for PA performance deviation from its typical behavior, is demonstrated, using the set-up within the mobile unit shown in Fig. 8. Only two probes for a minimum number of quasi-static power measurements over a narrow power range are required. The resulting adjustments of the 3-port representation, and consequently F, enable the PA linearity improvements summarized in Tables 1-2. Including a more precise output probe and an additional probe to measure the bias signal (such as the *Bias Control/Probe* in Fig. 20) allowed further PA linearity improvement.
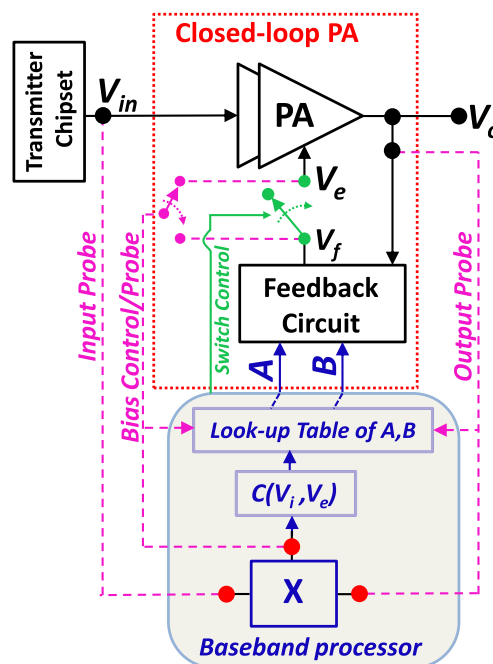

FIGURE 19. Measured gain vs P_{out}, V_{dyn} vs P_{out} with and without positive envelope feedback [12, Fig. 5].

VIII. DISCUSSION ON USE OF PROPOSED 3-PORT REPRESENTATION FOR EMBEDDED SELF-CALIBRATION

This section discusses the use of our proposed 3-port PA representation for implementing embedded self-calibration functions introduced for the first time in this paper, and intended for use within the mobile unit. One such application was extensively described in Section IV-D, that allowed adjusting, via embedded self-calibration, the pre-distortion applied to an open-loop PA to compensate against part-to-part variation of PA behavior. The open-loop case is briefly highlighted in this section, while a closed-loop PA application is discussed in greater detail.

A. EMBEDDED SELF-CALIBRATION OF OPEN-LOOP PA

As discussed earlier, the sequence comprising Steps 1-4 of Section III-B to extract the coefficients of polynomials G and P of our proposed 3-port representation (X in Fig. 1, Fig. 8), lends itself favorably for adoption by the RFIC PA manufacturer at an advanced engineering phase of the development. A single set of extracted coefficients, which describe the PA's typical behavior, may then be provided to a mobile equipment manufacturer as parameters of our proposed PA representation, for use in embedded self-calibration functions within the mobile unit that enable accounting for PA part-to-part variation.

FIGURE 20. Application of proposed 3-port representation for self-calibration embedded within the mobile unit applied to closed-loop PA under positive envelope feedback.

The example above describes one possible self-calibration function, and targets the open-loop PA's linearity. We now discuss the application of our proposed 3-port representation for embedded self-calibration of closed-loop PAs, for the specific case of the closed-loop PA with positive envelope feedback.

B. EMBEDDED SELF-CALIBRATION OF CLOSED-LOOP PA

Fig. 20 shows the set-up within the mobile unit for embedded self-calibration of the closed loop PA using positive envelope feedback. X refers to our proposed 3-port representation, the parameters of which gives the relationship between the signals at the nodes V_{in}, V_o and V_e for the typical open-loop PA. Along with this single set of parameters, the PA manufacturer may also provide to the mobile equipment manufacturer a single look-up table representing the typical transfer function

of the feedback circuit (Fig. 20), extracted through the steps described in Section VII-C. Knowing this single set of data, that represents parameter values associated to one given PA product, allows determining the value of A_{opt} (for optimum value of detector threshold) and B_{opt} (for optimum value of detector slope) that should be used for the typical closed-loop PA under positive envelope feedback.

For a different PA under closed-loop operation within a different mobile equipment, suitable adjustments in the values of A_{opt} and B_{opt} may be carried out to optimize linearity while ensuring stability. We now describe an embedded adjustment of the parameters of X and the look-up table stored in the baseband processor within the mobile unit in Fig. 20, to account for a performance deviation of the new PA compared to its typical behavior.

(i) The *Input Probe*, *Output Probe* and *Bias Control/Probe* in Fig. 20 are used to update the parameters of the open-loop PA representation X for the new PA, through the steps described in Section IV-D.

(ii) The updated parameters of X are used to update the conversion gain parameter $C(V_i, V_e)$ defined by (18). The new limit value on the feedback circuit's transfer function computed with (20) to ensure its stability is now known.

(iii) The *Output Probe* and the *Bias Control/Probe* are used to measure the RF signal V_o and the baseband signal V_f respectively, to determine the adjusted values of the feedback circuit's transfer function $f(A, B)$ (19). This accounts for part-to-part variation of the feedback circuit itself, and the look-up table of A, B is suitably updated.

(iv) The updated value of the parameters in X, the new limit value of $f(A, B)$ and the updated look-up table are now used to adjust the values of A_{opt} and B_{opt} for improved linearity of the new PA while guaranteeing its closed-loop stability, through the steps described in Section VII-E.

Once the adjusted A_{opt} and B_{opt} are set, the electronic switch control in Fig. 20 is used to close the positive envelope feedback loop for the new PA. The resulting closed-loop PA with positive envelope feedback is expected to have a gain profile that results in improved linearity performances, while ensuring PA stability.

C. OTHER APPLICATIONS

Beside the open-loop and closed-loop applications discussed above, our proposed 3-port PA representation for embedded self-calibration may be used to optimize other PA performances e.g. gain regulation in PAs that employ the switching ON or OFF of transistor arrays for efficiency improvement [16]. Such switching architectures may result in undesirable gain variations from one PA part to another. Using the simple probing circuitry as shown in Fig. 20 to measure the ratio between the input and output signals, the gain deviation may be cancelled through adjustment of the DC bias. Afterwards, PA linearity may be optimized following the procedure described in Section IV-C.

IX. CONCLUSION

This paper presents a 3-port representation of RFIC PAs under envelope-dependent dynamic biasing, based on complex polynomials that describe a combiner, a nonlinear baseband-to-RF converter and a nonlinear RF amplifying function. The proposed representation, extracted using multi-tone signals, allows predicting the dynamic biasing necessary to linearize the PA under multi-tone as well as modulated RF excitation signals. The paper also presents, for the first time, a novel embedded self-calibration technique for use within the transmitter front-end of the mobile unit when implementing envelope-dependent dynamic biasing of RFIC PAs. This self-calibration technique using the proposed 3-port representation enables the adjustment of the PA's dynamic biasing from one mobile unit to another, to account for part-to-part variation in PA behavior. The different tests that are presented, based on both simulation and experimental implementations, highlight the relative simplicity yet good accuracy of the proposed 3-port representation's characterization process compared to other PA representations, and its use for the embedded self-calibration of PA architectures using different open-loop and closed-loop envelope-dependent dynamic biasing techniques.

APPENDIXES
APPENDIX A

Centering the multi-tone measurements significantly aids in solving the system of equations in Step 1 and Step 4 of Section III-B. Mathematically, this translates into a minor modification of (14) as it is presented earlier into the form in (A1.1), where the additional term $k_{\omega_c + i\omega_x}$ refers to a constant complex number that accounts for centering the voltage measurements at the frequency tone $\omega_c + i\omega_x$.

$$v_o'(t) = \sum_{i=-u}^{u} (\boldsymbol{k_{\omega_c + i\omega_x}} + V_o'(\omega_c + i\omega_x)) \cdot cos((\omega_c + i\omega_x)\, t + \beta_{\omega_c + i\omega_x}) \quad \text{(A1.1)}$$

These additional $k_{\omega_c + i\omega_x}$ constants do not affect the extraction procedure described in Section III-B for the coefficients a_1, a_3, a_5 of polynomial G. This is because a_1, a_3, a_5 capture the nonlinear dependence of the PA's output signal on its input signal over the power range of interest, while $k_{\omega_c + i\omega_x}$ merely represents a constant offset value.

An example of the values of $k_{\omega_c + i\omega_x}$ for the test-case described in Section IV are given by (A1.2).

$$k_{\omega_c} = -0.03 - j \cdot 0.04,$$
$$k_{\omega_c + \omega_x} = -0.03 + j \cdot 0.12, \quad k_{\omega_c + 2\omega_x} = +0.03 + j \cdot 0.03$$
$$k_{\omega_c - \omega_x} = +0.06 - j \cdot 0.13, \quad k_{\omega_c - 2\omega_x} = -0.02 + j \cdot 0.02$$
$$\text{(A1.2)}$$

Additionally, frequency domain asymmetry of the PA's IMD$_3$ at high power levels is handled through a minor modification of the input signal V_a to the polynomial G as shown in (A2.1). The coefficient $b_{\omega_c + i\omega_x}$ is zero when there is no

IMD$_3$ asymmetry, but is a complex constant for power levels when IMD$_3$ asymmetry becomes significant.

$$
\begin{aligned}
v_a(t) &= (\sum_{i=-1}^{1} b_{\omega_c+i\omega_x} \cdot V_{in}(\omega_c + i\omega_x) \cdot \cos\left((\omega_c + i\omega_x)t + \theta_{\omega_c+i\omega_x}\right) \\
&+ \sum_{i=-s}^{s} (\sum_{q=1}^{m} \sum_{l=1}^{n} p_{iql}\{V_e(q) \cdot \cos(\phi_q)\}^l) \cdot e^{j(\omega_c+i\omega_x)t}
\end{aligned}
$$
(A2.1)

For example, the values of $b_{\omega_c+i\omega_x}$ for the test-case described in Section IV are given by (A2.2)

$$
\begin{aligned}
b_{\omega_c} &= 7.64 - j \cdot 2.45 \\
b_{\omega_c+\omega_x} &= 6.47 - j \cdot 5.10 \\
b_{\omega_c-\omega_x} &= 7.87 + j \cdot 0.79
\end{aligned}
$$
(A2.2)

It is useful to point out that the modifications given in Appendix A do not affect the order or the complexity of the proposed formulations presented in Section III.

APPENDIX B

For determining the expression of the PA's conversion gain from the bias node V_{ctrl} to the output node V_o in Fig. 18 using the proposed 3-port representation, the PA is excited with a single small-signal baseband-tone V_e at the bias node and a single RF-tone V_i at the input node. For determining this conversion gain, the value of the amplitudes only of the baseband bias signal and the PA's output envelope (both at frequency ω_x) is necessary, and there is no requirement to measure the absolute phase value of the signals at the nodes V_i, V_o and V_{ctrl} i.e their phase with respect to a single time reference. Therefore, these absolute values of the phase of the signals are ignored without any loss of generality for the formulations derived in this appendix, and the amplitudes only of V_i, V_o and V_e are considered. (6) and (8) therefore reduce to equations (A3) and (A4).

$$
v_i(t) = V_i(\omega_c) \cdot \cos(\omega_c t)
$$
(A3)
$$
v_e(t) = V_e \cdot \cos(\omega_x t)
$$
(A4)

Assuming a second-order polynomial for P gives expression (A5) for ΔV_a, where the number of tones are restricted to the three primary tones at frequencies ω_c, $\omega_c + \omega_x$ and $\omega_c - \omega_x$.

$$
\begin{aligned}
\Delta V_a(\omega_c) &= p_{011} \cdot V_e + p_{012} \cdot V_e^2 \\
\Delta V_a(\omega_c + \omega_x) &= p_{111} \cdot V_e + p_{112} \cdot V_e^2 \\
\Delta V_a(\omega_c - \omega_x) &= p_{-111} \cdot V_e + p_{-112} \cdot V_e^2
\end{aligned}
$$
(A5)

Here, p_{011}, p_{012}, p_{111} etc. refer to the coefficients of polynomial P. For example, consider the coefficient p_{-112}. Here the third index 2 represents that it captures the contribution of the 2nd-order term V_e^2 to the 1st side-tone $\Delta V_a(\omega_c - \omega_x)$ (given by index -1), V_e being the value of the $1 \cdot \omega_x$ frequency tone in the bias signal (given by index 1).

Using (A3), (A4) and (A5) gives the following unilateral expression for $v_a(t)$.

$$
\begin{aligned}
v_a(t) &= V_i(\omega_c) \cdot \cos(\omega_c t) + \left(p_{011} \cdot V_e + p_{012} \cdot V_e^2\right) \cdot \cos(\omega_c t) \\
&+ \left(p_{111} \cdot V_e + p_{112} \cdot V_e^2\right) \cdot \cos\left((\omega_c + \omega_x)t\right) \\
&+ \left(p_{-111} \cdot V_e + p_{-112} \cdot V_e^2\right) \cdot \cos\left((\omega_c - \omega_x)t\right)
\end{aligned}
$$

i.e.

$$
\begin{aligned}
v_a(t) &= p_0 \cdot \cos(\omega_c t) + p_1 \cdot \cos\left((\omega_c + \omega_x)t\right) \\
&+ p_{-1} \cdot \cos\left((\omega_c - \omega_x)t\right)
\end{aligned}
$$
(A6.1)

where

$$
\begin{aligned}
p_0 &= V_i(\omega_c) + V_e \cdot (p_{011} + p_{012} \cdot V_e) \\
p_1 &= V_e \cdot (p_{111} + p_{112} \cdot V_e) \\
p_{-1} &= V_e \cdot (p_{-111} + p_{-112} \cdot V_e)
\end{aligned}
$$
(A6.2)

Applying (A6.1) as input to the 5th-order polynomial G and considering only the resulting amplitudes at the three primary frequency tones shown in Fig. 18 gives the following value of the output signal V_o.

$$
\begin{aligned}
v_o(t) &= r_0 \cdot \cos(\omega_c t) + r_1 \cdot \cos\left((\omega_c + \omega_x)t\right) + r_{-1} \\
&\cdot \cos\left((\omega_c - \omega_x)t\right)
\end{aligned}
$$
(A7.1)

where

$$
\begin{aligned}
r_0 = a_1 \cdot p_0 + a_3 &\cdot \left\{\frac{3}{4}p_0^3 + \frac{3}{2}p_0 p_1^2 + \frac{3}{2}p_0 p_{-1}^2 + \frac{3}{2}p_0 p_1 p_{-1}\right\} \\
+ a_5 &\cdot \left\{\frac{5}{8}p_0^5 + \frac{15}{8}p_0 p_1^4 + \frac{15}{8}p_0 p_{-1}^4 + \frac{15}{4}p_0^3 p_1^2\right. \\
&+ \frac{15}{4}p_0^3 p_{-1}^2 + \frac{15}{4}p_0 p_1^3 p_{-1} + \frac{15}{4}p_0 p_1 p_{-1}^3 \\
&\left. + \frac{15}{2}p_0 p_1^2 p_{-1}^2 + 5p_0^3 p_1 p_{-1}\right\}
\end{aligned}
$$
(A7.2)

$$
\begin{aligned}
r_1 = a_1 \cdot p_1 + a_3 &\cdot \left\{\frac{3}{4}p_1^3 + \frac{3}{2}p_1 p_0^2 + \frac{3}{4}p_{-1}p_0^2 + \frac{3}{2}p_1 p_{-1}^2\right\} \\
+ a_5 &\cdot \left\{\frac{5}{8}p_1^5 + \frac{15}{4}p_0^2 p_1^3 + \frac{15}{8}p_0^2 p_{-1}^3 + \frac{15}{4}p_1^3 p_{-1}^2\right. \\
&+ \frac{15}{8}p_1 p_0^4 + \frac{15}{8}p_1 p_{-1}^4 + \frac{15}{2}p_0^2 p_1 p_{-1}^2 + \frac{5}{4}p_0^4 p_{-1} \\
&\left. + \frac{45}{8}p_0^2 p_1^2 p_{-1}\right\}
\end{aligned}
$$
(A7.3)

$$
\begin{aligned}
r_{-1} = a_1 \cdot p_{-1} + a_3 &\cdot \left\{\frac{3}{4}p_{-1}^3 + \frac{3}{2}p_{-1}p_0^2 + \frac{3}{4}p_1 p_0^2 + \frac{3}{2}p_{-1}p_1^2\right\} \\
+ a_5 &\cdot \left\{\frac{5}{8}p_{-1}^5 + \frac{15}{4}p_0^2 p_{-1}^3 + \frac{15}{8}p_0^2 p_1^3 + \frac{15}{4}p_{-1}^3 p_1^2\right. \\
&+ \frac{15}{8}p_{-1}p_0^4 + \frac{15}{8}p_{-1}p_1^4 + \frac{15}{2}p_0^2 p_{-1}p_1^2 + \frac{5}{4}p_0^4 p_1 \\
&\left. + \frac{45}{8}p_0^2 p_{-1}^2 p_1\right\}
\end{aligned}
$$
(A7.4)

The small asymmetry in the two output side-tones of amplitude r_1 and r_{-1}, due to the higher-order terms as shown in their expansions given by (A7.3) and (A7.4), has a negligible effect on the output envelope amplitude, whose value is then given by (A8).

$$Env(V_o) \approx 2r_1 \approx 2r_{-1} \qquad (A8)$$

The PA's conversion gain (C) from the bias node to the output node is now given by (A9).

$$C(V_i, V_e) = \frac{Env(V_o)}{V_e} \approx \frac{2r_1}{V_e} \qquad (A9)$$

A better understanding of the contribution of V_i and V_e to the conversion gain given by (A9) can be obtained by simplifying (A9) after its expansion. For this purpose, coefficient a_5 is set to zero and only the first few significant terms are considered. The resulting simplified expression is given by (A10), and its compact representation by (A11).

$$
\begin{aligned}
C(V_i, V_e) = {} & a_1 \cdot (p_{111} + p_{112} \cdot V_e) + \frac{3}{2} \cdot a_3 \cdot V_i^2 \\
& \cdot \left(p_{111} + \frac{1}{2}p_{-111} \right) + 3 \cdot a_3 \cdot V_i \cdot V_e \cdot p_{011} \\
& \cdot \left(p_{111} + \frac{1}{2}p_{-111} \right) + \frac{3}{2} \cdot a_3 \cdot V_i^2 \cdot V_e \\
& \cdot \left(p_{112} + \frac{1}{2}p_{-112} \right) + 3 \cdot a_3 \cdot V_i \cdot V_e^2 \\
& \cdot \left(p_{011} \cdot p_{112} + \frac{1}{2}p_{011} \cdot p_{-112} \right. \\
& + p_{012} \cdot p_{111} + \frac{1}{2}p_{012} \cdot p_{-111} \Big) \\
& + \frac{3}{2} \cdot a_3 \cdot V_e^2 \cdot \left(p_{011}^2 \cdot p_{111} + \frac{1}{2}p_{011}^2 \cdot p_{-111} \right. \\
& \left. + p_{-111}^2 \cdot p_{111} + \frac{1}{2}p_{111}^3 \right) + \dots \qquad (A10)
\end{aligned}
$$

i.e.

$$
\begin{aligned}
C(V_i, V_e) = {} & a_1 \cdot p_{111} + a_1 \cdot p_{112} \cdot V_e + a_3 \cdot f_1(V_i) \\
& + a_3 \cdot f_2(V_e) + a_3 \cdot f_3(V_i, V_e) \qquad (A11)
\end{aligned}
$$

where $f_1(V_i)$, $f_2(V_e)$, $f_3(V_i, V_e)$ are nonlinear functions. $C(V_i, V_e)$ therefore consists of a constant term composed of the product of the 1st-order G coefficient a_1 and the 1st-order P coefficient p_{111}, along with other higher-order functions of V_i and V_e.

ACKNOWLEDGMENT

REFERENCES

[1] K. W. Lau, Q. Xue, and C. H. Chan, "A novel biasing technique for low adjacent channel power in microwave power amplifiers," in *Proc. Asia–Pacific Microw. Conf.*, Bangkok, Thailand, Dec. 2007, pp. 1–4.

[2] T. H. Miers and V. A. Hirsch, "A thorough investigation of dynamic bias on linear GaAs FET power amplifier performance," in *IEEE MTT-S Microw. Symp. Dig.*, Albuquerque, NM, USA, Jun. 1992, vol. 2, pp. 537–540.

[3] J. Nam and B. Kim, "The Doherty power amplifier with on-chip dynamic bias control circuit for handset application," *IEEE Trans. Microw. Theory Techn.*, vol. 55, no. 4, pp. 633–642, Apr. 2007.

[4] B. Sahu and G. A. Rincon-Mora, "A high efficiency WCDMA RF power amplifier with adaptive, dual-mode buck-boost supply and bias-current control," *IEEE Microw. Wireless Compon. Lett.*, vol. 17, no. 3, pp. 238–240, Mar. 2007.

[5] S. Forestier, P. Bouysse, R. Quere, A. Mallet, J. M. Nebus, and L. Lapierre, "Joint optimization of the power-added efficiency and the error-vector measurement of 20-GHz pHEMT amplifier through a new dynamic bias-control method," *IEEE Trans. Microw. Theory Techn.*, vol. 52, no. 4, pp. 1132–1141, Apr. 2004.

[6] N. Constantin, "Dynamic biasing system for an amplifier," U.S. Patent 7 719 354 B2, May 18, 2010.

[7] N. Deltimple, L. Leyssenne, E. Kerhervé, Y. Deval, and D. Belot, "Dynamic biasing techniques for RF power amplifier linearity and efficiency improvement," in *Proc. IEEE Int. Conf. Integr. Circuit Design Technol.*, Grenoble, France, Jun. 2010, pp. 232–235.

[8] P. Medrel, T. Reveyrand, A. Martin, P. Bouysse, J.-M. Nébus, and J. Sombrin, "Time domain envelope characterization of power amplifiers for linear and high efficiency design solutions," in *Proc. WAMICON*, Orlando, FL, USA, Apr. 2013, pp. 1–6.

[9] F. F. Tafuri, D. Sira, O. K. Jensen, and T. Larsen, "Efficiency enhancement of an envelope tracking power amplifier combining supply shaping and dynamic biasing," in *Proc. Eur. Microw. Conf.*, Nuremberg, Germany, Oct. 2013, pp. 1491–1494.

[10] P.-C. Wang, "A 2.4-GHz +25 dBm P-1 dB linear power amplifier with dynamic bias control in a 65-nm CMOS process," in *Proc. 34th Eur. Solid-State Circuits Conf. (ESSCIRC)*, Edinburgh, U.K., Sep. 2008, pp. 490–493.

[11] K. Onizuka, K. Ikeuchi, S. Saigusa, and S. Otaka, "A 2.4 GHz CMOS Doherty power amplifier with dynamic biasing scheme," in *Proc. IEEE Asian Solid State Circuits Conf. (A-SSCC)*, Kobe, Japan, Nov. 2012, pp. 93–96.

[12] S. Sharma, Y. Soliman, and N. G. Constantin, "Positive envelope feedback for linearity improvement in RFIC PAs," in *Proc. 27th Int. Conf. Radioelektronika*, Apr. 2017, pp. 1–5.

[13] S. Kang, D. Baek, and S. Hong, "A 5-GHz WLAN RF CMOS power amplifier with a parallel-cascoded configuration and an active feedback linearizer," *IEEE Trans. Microw. Theory Techn.*, vol. 65, no. 9, pp. 3230–3244, Sep. 2017.

[14] B. K. Thangarasu, K. Ma, and K. S. Yeo, "A 0.029 mm² 8 Gbit/s current-mode AGC amplifier with reconfigurable closed-loop control in 65 nm CMOS," in *IEEE MTT-S Int. Microw. Symp. Dig.*, Honolulu, HI, USA, Jun. 2017, pp. 107–110.

[15] M. El-Shennawy, N. Joram, and F. Ellinger, "A 55 dB range gain interpolating variable gain amplifier with improved offset cancellation," in *Proc. 12th Conf. Ph.D. Res. Microelectron. Electron. (PRIME)*, Lisbon, Portugal, Jun. 2016, pp. 1–4.

[16] J. Joung, C. K. Ho, and S. Sun, "Power amplifier switching (PAS) for energy efficient systems," in *IEEE Wireless Commun. Lett.*, vol. 2, no. 1, pp. 14–17, Feb. 2013.

[17] Y. Yang, J. Yi, J. Nam, and B. Kim, "Behavioral modeling of high power amplifiers based on measured two-tone transfer characteristics," *Microw. J.*, vol. 43, pp. 90–104, Dec. 2000.

[18] G. P. Gibiino, G. Avolio, D. M. M.-P. Schreurs, A. Santarelli, and F. Filicori, "A three-port nonlinear dynamic behavioral model for supply-modulated RF PAs," *IEEE Trans. Microw. Theory Techn.*, vol. 64, no. 1, pp. 133–147, Jan. 2016.

[19] J. C. Pedro and S. A. Maas, "A comparative overview of microwave and wireless power-amplifier behavioral modeling approaches," *IEEE Trans. Microw. Theory Techn.*, vol. 53, no. 4, pp. 1150–1163, Apr. 2005.

[20] A. S. Tehrani, H. Cao, T. Eriksson, M. Isaksson, and C. Fager, "A comparative analysis of the complexity/accuracy tradeoff in power amplifier behavioral models," *IEEE Trans. Microw. Theory Techn.*, vol. 58, no. 6, pp. 1510–1520, Jun. 2010.

[21] G. P. Gibiino, A. Santarelli, D. Schreurs, and F. Filicori, "Two-input nonlinear dynamic model inversion for the linearization of envelope-tracking RF PAs," in *IEEE Microw. Wireless Compon. Lett.*, vol. 27, no. 1, pp. 79–81, Jan. 2017.

[22] S. A. Maas, *Nonlinear Microwave and RF Circuits*, 2nd ed. Norwood, MA, USA: Artech House, 2003, pp. 235–250.

[23] Nicolas G. Constantin and S. Sharma, "Power amplifier linearizing module and power amplifier system equipped therewith," Provisional Patent Appl. 62/899 793 PR, Sep. 13, 2019.

[24] H. Ku and J. S. Kenney, "Estimation of error vector magnitude using two-tone intermodulation distortion measurements," in *IEEE MTT-S Int. Microw. Symp. Dig.*, Phoenix, AZ, USA, vol. 1, May 2001, pp. 17–20.

[25] N. B. De Carvalho and J. Pedro, "Compact formulas to relate ACPR and NPR to two-tone IMR and IP3," *Microw. J.*, vol. 42, no. 12, p. 70, Dec. 1999.

[26] B. Park, S. Jin, D. Jeong, J. Kim, Y. Cho, K. Moon, and B. Kim, "Highly linear mm-Wave CMOS power amplifier," *IEEE Trans. Microw. Theory Techn.*, vol. 64, no. 12, pp. 4535–4544, Dec. 2016.

[27] S. Sharma and N. G. Constantin, "Formulations for the estimation of IMD levels in an envelope feedback RFIC amplifier: An extension to dynamic AM and PM behavior," *IEEE Trans. Comput.-Aided Design Integr. Circuits Syst.*, vol. 32, no. 12, pp. 2019–2023, Dec. 2013.

[28] C. J. Clark, C. P. Silva, A. A. Moulthrop, and M. S. Muha, "Power-amplifier characterization using a two-tone measurement technique," *IEEE Trans. Microw. Theory Techn.*, vol. 50, no. 6, pp. 1590–1602, Jun. 2002.

[29] J. C. Pedro, N. B. Carvalho, C. Fager, and J. A. Garcia, "Linearity versus efficiency in mobile handset power amplifiers: A battle without a loser," in *Proc. Microw. Eng. Eur.*, Aug. 2004, pp. 1–6.

[30] C. Fager, J. C. Pedro, N. B. de Carvalho, H. Zirath, F. Fortes, and M. J. Rosario, "A comprehensive analysis of IMD behavior in RF CMOS power amplifiers," *IEEE J. Solid-State Circuits*, vol. 39, no. 1, pp. 24–34, Jan. 2004.

[31] *High-Power (+19 dBm) 802.11ac WLAN Power Amplifier With Integrated Power Detector*, document SE5003L1-R, Skyworks Solutions, Oct. 2013.

[32] S. Sharma and N. G. Constantin, "Amplifier architecture using positive envelope feedback," U.S. Patent 15/862 914, Jan. 2018.

[33] S. Sharma and N. G. Constantin, "Apparatus and methods for power amplifiers with positive envelope feedback," U.S. Patent 15/956 443, Apr. 2018.

SMARJEET SHARMA (S'10) received the B.E. degree (Hons.) in electrical and electronics engineering from the Birla Institute of Technology and Science (BITS), Pilani, India, in 2012. He is currently pursuing the Ph.D. degree in electrical engineering, as part of the M.A.Sc.–Ph.D. integrated program with the École de Technologie Supérieure (ÉTS)–University of Quebec, Canada.

He received the NTSE Scholarship from NCERT, Government of India, in 2006, and the MITACS-Globalink Scholarship for undergraduate research in Canada, in 2011. He is a recipient of the M.A.Sc.–Ph.D. Scholarship from the ÉTS and the MITACS-Accelerate Fellowship.

NICOLAS G. CONSTANTIN (SM'2019) received his B.Eng. degree in 1989 from the École de Technologie Supérieure (ÉTS)–University of Quebec, Canada, his M.A.Sc. degree in 1994 from the École Polytechnique de Montréal, Canada, and his Ph.D. degree in 2009 from McGill University, Canada, all in electrical engineering.

He is currently an Associate Professor at the ÉTS, Montreal, Canada. From 1989 to 1992 he worked in the design of microwave transceivers for point to point radio links. From 1996 to 1998 he worked as an RF Design Engineer at NEC, in the development of RF and microwave transceivers for mobile telephony. From 1998 to 2002 he was a Senior Design Engineer at Skyworks Solutions, Inc., California, USA, where he developed GaAs HBT RFIC PAs for wireless communications. At Skyworks he was also actively involved in research on smart biasing and efficiency improvement techniques for RFIC PAs, and he is the author of several patents on the subject. He was the recipient of a Doctoral Scholarship from the Natural Science and Engineering Research Council (NSERC) of Canada, and a Doctoral Scholarship from the ÉTS. His primary research interests are in the design and test of Analog, RF & Millimeter-wave ICs and Front-End modules for wireless communications. He conducts research in collaboration with major companies in the wireless communication and aerospace industry.

• • •